AD-A095 356 SRI INTERNATIONAL MENLO PARK CA F/G 17/5
LIDAR OBSERVATIONS AT 0.7 MICROMETERS AND 10.6 MICROMETERS WAVE--ETC(U)
NOV 80 E E UTHE DAAG29-77-C-0001
UNCLASSIFIED ERADCOM/ASL-CR-80-0001-1 NL

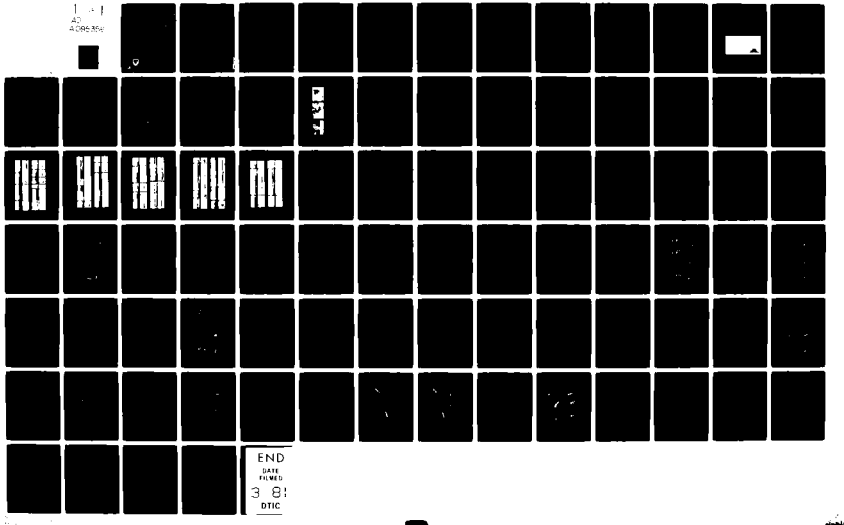

END
DATE FILMED
3 81
DTIC

ASL-CR-80-0001-1

AD

Reports Control Symbol
OSD - 1366

12

LIDAR OBSERVATIONS AT 0.7-μm AND 10.6-μm WAVELENGTHS DURING SMOKE WEEK II

Final Report

NOVEMBER 1980

LEVEL II

Prepared by
EDWARD E. UTHE

SRI INTERNATIONAL
333 Ravenswood Avenue
Menlo Park, CA 94025

Prepared for

US ARMY RESEARCH OFFICE
Geosciences Division
Research Triangle Park, NC 27709

and

US ARMY ATMOSPHERIC SCIENCES LABORATORY
White Sands Missile Range, NM 88002

Contract No. DAAG29-77-C-0001

Contract Monitor: Jagir Randhawa

Approved for public release; distribution unlimited

US Army Electronics Research and Development Command
Atmospheric Sciences Laboratory
White Sands Missile Range, NM 88002

NOTICES

Disclaimers

The findings in this report are not to be construed as an official Department of the Army position, unless so designated by other authorized documents.

The citation of trade names and names of manufacturers in this report is not to be construed as official Government indorsement or approval of commercial products or services referenced herein.

Disposition

Destroy this report when it is no longer needed. Do not return it to the originator.

SECURITY CLASSIFICATION OF THIS PAGE (When Data Entered)

REPORT DOCUMENTATION PAGE

READ INSTRUCTIONS BEFORE COMPLETING FORM

1. REPORT NUMBER: ASL-CR-80-0001-1	2. GOVT ACCESSION NO.: AD-A095356
3. RECIPIENT'S CATALOG NUMBER:	
4. TITLE (and Subtitle): LIDAR OBSERVATIONS AT 0.7-μm AND 10.6-μm WAVELENGTHS DURING SMOKE WEEK II. Micrometers	5. TYPE OF REPORT & PERIOD COVERED: R&D Final Report
	6. PERFORMING ORG. REPORT NUMBER: SRI Project 5862
7. AUTHOR(s): Edward E. Uthe	8. CONTRACT OR GRANT NUMBER(s): DAAG29-77-C-0001
9. PERFORMING ORGANIZATION NAME AND ADDRESS: SRI International, 333 Ravenswood Avenue, Menlo Park, California 94025	10. PROGRAM ELEMENT, PROJECT, TASK AREA & WORK UNIT NUMBERS: Task No. 1L162111AH71-23
11. CONTROLLING OFFICE NAME AND ADDRESS: US Army Electronics Research and Development Command, Adelphi, Maryland 20783	12. REPORT DATE: November 1980
	13. NUMBER OF PAGES: 92
14. MONITORING AGENCY NAME & ADDRESS (if different from Controlling Office): US Army Atmospheric Sciences Laboratory, White Sands Missile Range, New Mexico 88002	15. SECURITY CLASS. (of this report): UNCLASSIFIED
	15a. DECLASSIFICATION/DOWNGRADING SCHEDULE

16. DISTRIBUTION STATEMENT (of this Report)

Approved for public release; distribution unlimited.

ERADCOM/ASL

17. DISTRIBUTION STATEMENT (of the abstract entered in Block 20, if different from Report)

18. SUPPLEMENTARY NOTES

19. KEY WORDS (Continue on reverse side if necessary and identify by block number)

Lidar	Dense dust and smoke
Military smoke	Multiwavelength lidar
Optical properties	Eglin AFB
Optical backscatter	Fog oil
Optical transmission	

20. ABSTRACT (Continue on reverse side if necessary and identify by block number)

A 10.6-μm wavelength lidar was operated by the U.S. Army Atmospheric Sciences Laboratory and a 0.7-μm wavelength lidar (Mark IX) was operated by SRI International to observe smoke and dust clouds generated during Smoke Week II at Eglin AFB from 6 through 16 November 1978. →

DD FORM 1 JAN 73 1473 EDITION OF 1 NOV 65 IS OBSOLETE

SECURITY CLASSIFICATION OF THIS PAGE (When Data Entered)

410281

20. ABSTRACT (cont)

The lidars observed cloud backscatter along horizontal paths that were nearly coincident with those observed by visible and infrared transmissometers operated by the Dugway Proving Ground. The lidar observed paths were terminated with a passive reflector so that time-dependent transmission over the lidar-to-target path could be evaluated from lidar observed target returns. Backscatter signatures for both lidars were digitized and recorded on magnetic tape using the Mark IX lidar data processing system.

Recorded lidar data were used to generate intensity-modulated TV displays depicting cloud structure along lidar observed paths as a function of time. These displays were used to choose sixteen Smoke Week II trials for quantitative analysis in terms of cloud attenuation and path-integrated backscatter.

Transmissions derived from lidar target returns agreed very well with transmissometer records, except for phosphorus events for which the lidar values were greater by as much as an order of magnitude. This discrepancy can be explained because the transmissometer paths were nearer to the surface than the lidar paths and other observations indicated that phosphorus clouds greatly decrease in optical density in the vertical.

Relationships between path-integrated backscatter and optical depth were investigated as possible means of developing a technique for evaluation of optical density for slant paths through aerosol clouds at various downwind distances from the source. Plots of integrated backscatter as a function of optical depth showed a large degree of scatter and indicated nonlinear relationships. The most scatter and nonlinear behavior were observed for oil fog followed by phosphorus and HC smoke, while the least scatter and most linear results were obtained for dust and experimental particle clouds. Nonlinear expressions were evaluated for data from several trials and these were used along with lidar observed backscatter to compute time-dependent transmission functions. These results relate fairly well with Dugway transmission records, indicating that single-ended lidar observations can be used to estimate path-integrated cloud optical density.

Two-wavelength lidar results for different aerosol types were consistent with previously observed results. Attenuation and backscatter were greater at the visible wavelength than at the infrared wavelength for HC and phosphorus smoke clouds but nearly equal to infrared values for dust clouds. For experimental particle clouds, the attenuation was nearly equal at the two wavelengths, but larger backscatter was observed at the infrared wavelength. For oil fog the attenuation was much greater at the visible wavelength, while backscatter was about equal at the two wavelengths.

CONTENTS

ILLUSTRATIONS

TABLES

ACKNOWLEDGMENTS

This research project was funded by the U.S. Army Research Office (ARO), Geosciences Division. Additional support was received from the U.S. Army Atmospheric Sciences Laboratory (ASL).

The author acknowledges the assistance of Jan van der Laan and Norm Nielsen during the data collection and John Livingston and Janet Carr during the data analysis program. Dr. J. S. Randhawa of ASL provided assistance throughout the study. The author also acknowledges helpful discussions on the method of approach and progress of this work with Dr. A. Dodd and Dr. L. Albert of ARO. Finally, the efforts of personnel from the Office of the Project Manager, Smoke/Obscurants during Smoke Week II were greatly appreciated.

I BACKGROUND

The unique capabilities of the lidar technique for observation of the atmosphere over remote distances has been well documented (Collis and Russell, 1976). The use of lidar to quantitatively describe aerosol, cloud, and precipitation distributions has been discussed by Uthe (1978). For example, Figure 1 presents a lidar-derived vertical cross section through a smoke plume that provides information on plume location, dimension, and relative particulate density distributions. However, the remote evaluation of absolute optical and physical density of an atmospheric scattering volume by use of lidar is normally limited to only special cases, and the accuracy of derived density values typically depends on the appropriateness of assumptions needed for various solution techniques. Although unique density values cannot be obtained in most cases because of uncertainties in particle characteristics (size, shape, and composition), the lidar may provide better estimates of density than

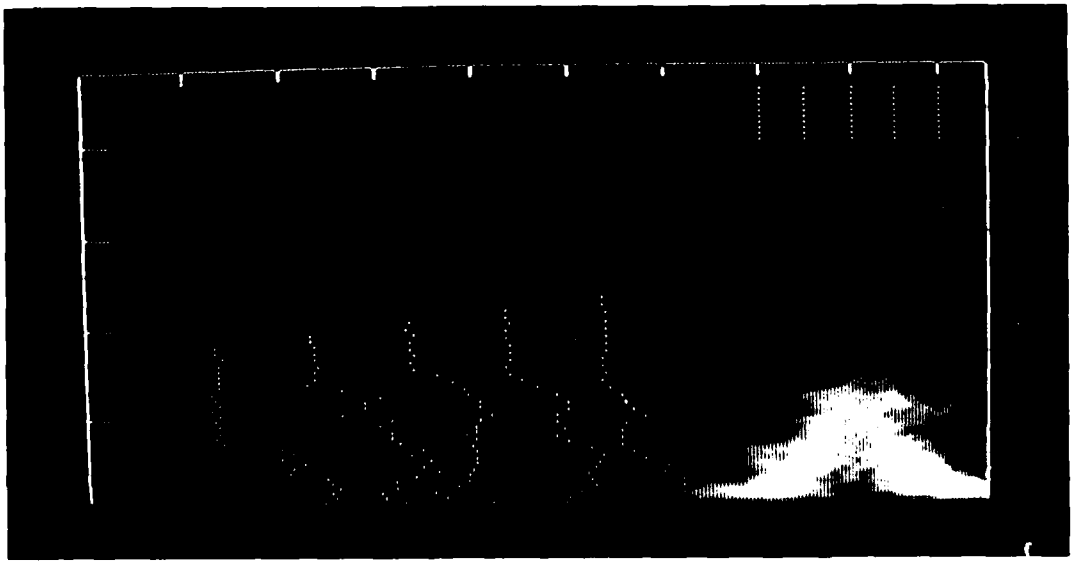

SA-4797-21

FIGURE 1 EXAMPLE OF COMPUTER-GENERATED VERTICAL PLUME DENSITY PROFILES

Lidar is located at lower left corner. The height and distance scale is 75 m/div. Plume vertical concentrations (relative to clear air with a scale of 10 dB/div) are plotted at the lower left and the horizontal position associated with each profile is plotted in the upper right.

by using in situ sampling methods when evaluations are made over extended atmospheric paths or volumes, as in the case of cross-plume integrated density for the plume shown in Figure 1. This is especially true for aerosol clouds that have large spatial and temporal variability. The recent development and use of digital data collection systems capable of processing the large data bases that can be produced by the lidar technique encourage reexamination of the possibility of useful quantitative density evaluations over remote areas.

SRI International (SRI) was awarded a project by the Army Research Office (ARO) to develop and evaluate digital lidar techniques for the remote evaluation of optical and physical densities of aerosol, cloud, and precipitation. Soon after this award, several Army development groups asked to have this program directed primarily towards the evaluation of lidar for remote observation of dense smoke and dust clouds used for obscurant purposes. The dense aerosol cloud problem was particularly challenging because of large attenuation and multiple-scattering effects. Also, the study of these clouds was appealing because scheduled experiments would provide extensive measurements of particle characterization and aerosol density for input to lidar signature analysis and for evaluation of lidar derived quantities. Transmissometer techniques were being used to evaluate cloud density along near-surface horizontal paths, but no technique was available for evaluating three-dimensional density distributions. Therefore, the successful development of a single-ended technique for remote cloud characterization could greatly extend the data base that was being collected by the Army.

Consideration of Army requirements led to the development of a prototype CO_2 (10.6-μm wavelength) lidar system. The system was interfaced with the SRI Mark IX lidar (0.7-μm wavelength) digital data system so that two-wavelength observations could be conducted in a near optimum manner, e.g., over nearly equal observational paths. The two-wavelength lidar system participated in a series of smoke tests conducted at the Dugway Proving Ground during September 1977. The results of this program were presented in Technical Report 1 (Uthe, 1978). Basically, it was shown that aerosol type (smoke or dust) strongly affected the wavelength dependence of backscatter and attenuation and that experimental results were consistent with previously derived theoretical data.

Based on the Dugway results, the U.S. Army Atmospheric Sciences Laboratory procured from SRI an improved version of the CO_2 lidar for further application to scheduled smoke and dust tests. Description of this system was detailed in Technical Report 2 issued on this project (van der Laan, 1979).

The ASL CO_2 lidar and the SRI Mark IX lidar systems were interfaced for optimum two-wavelength observations and data recording. This system participated in the Dusty Infrared Test 1 (DIRT-1) exercises conducted at White Sands Missile Range during October 1978. The data collected were consistent with the Dugway results, i.e., attenuation and backscatter at 0.7- and 10.6-μm wavelengths were about equal for dust aerosols but much greater at 0.7 μm than at 10.6 μm for smoke aerosols. Results of the DIRT-1 tests were reported in Technical Report 3 (van der Laan, 1979).

The interfaced ASL 10.6-μm wavelength lidar and the SRI 0.7-μm wavelength lidar system participated in the Smoke Week II experiments conducted at Eglin AFB during November 1978. A large data base on the transmission and scattering of various smoke and dust aerosols was obtained. A comprehensive data analysis program funded jointly by ARO and ASL was planned to demonstrate the equivalence between lidar and transmissometer derived transmissions. The program also evaluated the possibility of estimating transmission from lidar backscatter data so that cloud transmission over nonhorizontal paths could be evaluated during future programs. This report serves as a final report on this project and presents results obtained from the Smoke Week II experiments.

II EQUIPMENT AND PROCEDURES

The following descriptions outline the equipment and procedures used during the Smoke Week II program. Figure 2 illustrates the general experimental configuration, which is similar to that used during the Dugway and DIRT-1 tests reported earlier. The Smoke Week II lidar program has been described by Randhawa and Ballard (1979).

A. ASL Lidar

Specifications for the ASL 10.6-μm wavelength lidar system are given in Table 1. A detailed system description was presented by van der Laan (1979). Basically, the system is made up of two major components: a pulsed CO_2 laser that generates a very short, high peak power infrared (IR) pulse transmission, and a narrow field-of-view optical receiver that collects the backscattered energy and directs the signal to an IR detector. After detection and logarithmic amplification, the signal is digitized by a high-speed transient recorder that provides range-resolved backscatter amplitude data output in both digital and digitally reconstructed analog (DAC) formats. The digital output is primarily intended for recording and processing use while the DAC output is useful in observing the real-time backscatter returns. A functional diagram of the ASL lidar is shown in Figure 3.

B. Mark IX Lidar

The Mark IX lidar system is a self-contained mobile system operating at the ruby wavelength of 0.6943 μm. Details of the system and specifications are shown in Figure 4.

A principal feature of the Mark IX system is its digital data recording, processing, and display system for real-time viewing of range-resolved backscatter data in both A-scope and range-time-intensity (RTI) presentations. Details of the data system have been presented by Uthe and Allen (1975). The recorded data can be processed on the Mark IX system's computer (PDP-11) or reformatted for processing on a large, more versatile computer system. Processing by the lidar computer is used for display of data in pictorial TV format as shown in Figure 1, while processing by a large computer is used to take advantage of more efficient software routines applied to large data bases.

In addition to lidar data, the Mark IX is equipped with an integrating nephelometer that measures the in situ aerosol scattering coefficient. These data are also recorded on magnetic tape for post-event analysis.

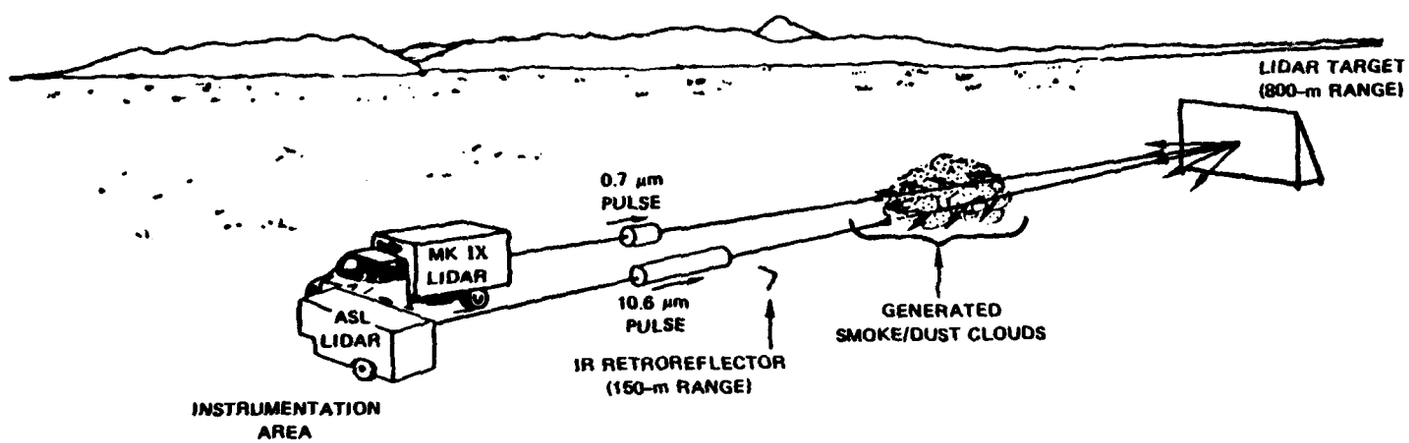

FIGURE 2 EXPERIMENTAL CONFIGURATION FOR TWO-WAVELENGTH LIDAR OBSERVATIONS DURING SMOKE WEEK II

Table 1

ASL LIDAR SPECIFICATIONS

System Component	Specification	Comments
Transmitter		
Manufacturer	Lumonics Research Ltd., Model TEA-101-2	
Type	CO_2	
Wavelength	10.6 μm	
Beam diameter	3.1 cm	
Beam divergence	1.2 mrad	
Operation	pulsed	
Energy	250 mJ	No nitrogen gas mix
Pulse width	75 ns (FWHM)	
PRF (maximum)	1 pps	
Receiver		
Telescope	12-inch (30 cm), Newtonian	LDV primary
Field of view	1.23 mrad	
Detector	Honeywell Associates; HgCdTe photodiode; $D^* = 1.3 \times 10^{10}$ cmHz$^{\frac{1}{2}}$W^{-1}; 100 MHz BW	LN_2-cooled
Postamplifier	Linear: 26 dB gain, 100 MHz BW	van der Laan (1979)
	Log: tangential sensitivity -111 dBr; ±0.5 dB linearity over 80-dB range; 15-ns rise time	van der Laan (1979)

C. Two-Wavelength Lidar Interface

The ASL lider system was not equipped with a recording capability, as its associated computer van was being utilized on other ASL programs.* To provide a processing capability during the Smoke Week II program, the ASL lidar backscatter data were recorded on the Mark IX lidar data system on an alternate record basis with backscatter signatures produced by the

*A dedicated data system has recently been added to the ASL lidar system.

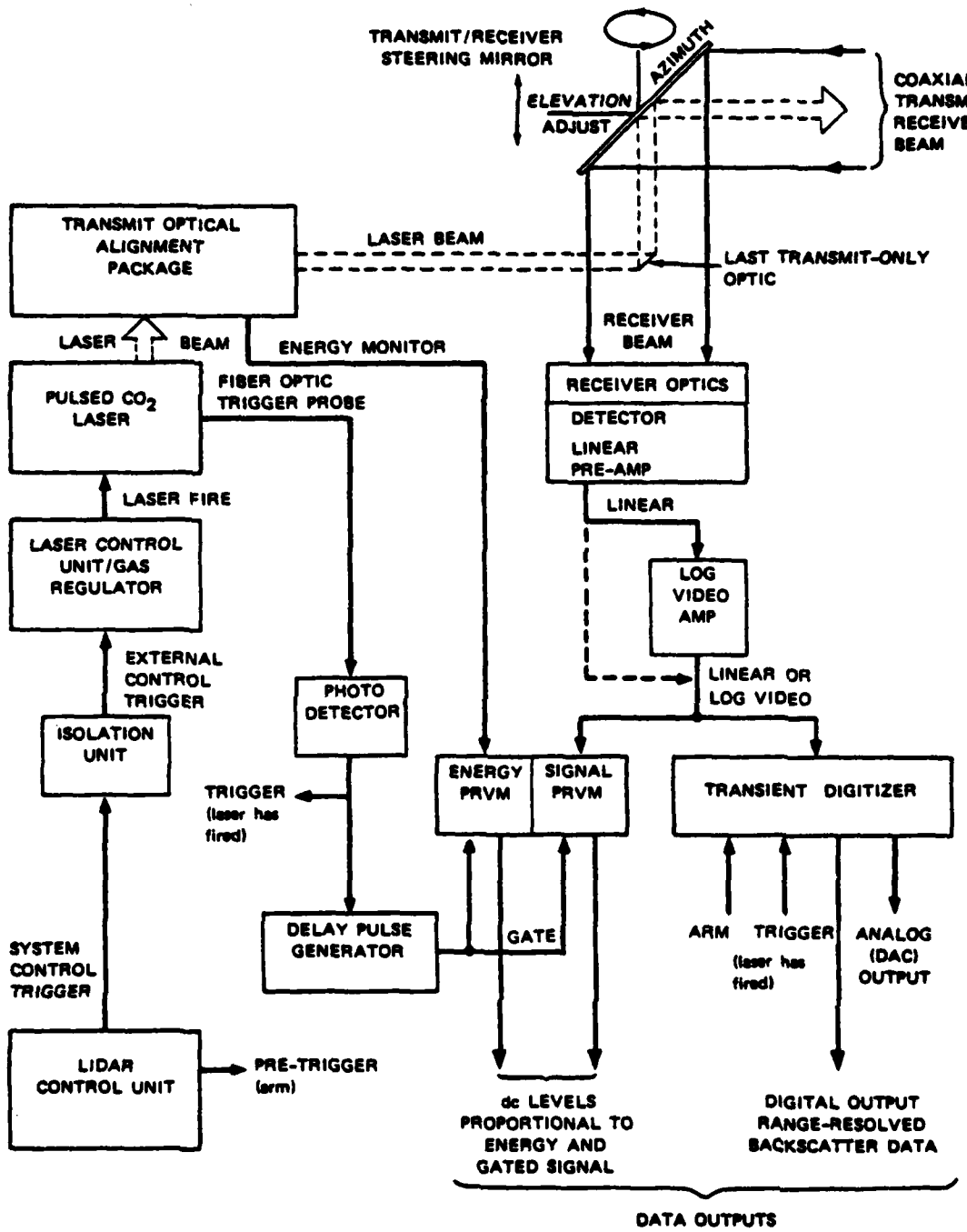

FIGURE 3 ASL LIDAR FUNCTIONAL DIAGRAM

(a) MARK IX LIDAR VAN

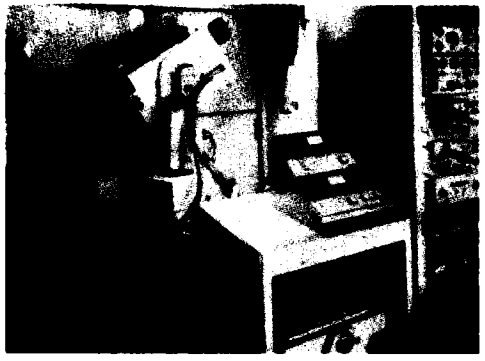

(b) ANALOG DATA AND FIRE CONTROL ELECTRONICS

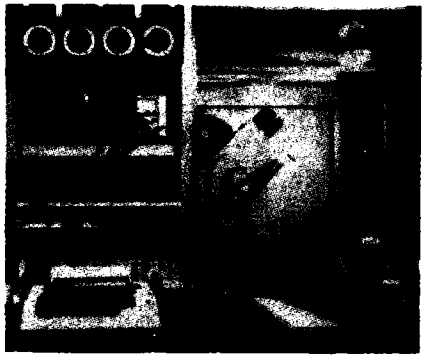

(c) DIGITAL DATA ELECTRONICS AND TV DISPLAY

EXTERIOR AND INTERIOR VIEWS OF THE LIDAR VAN

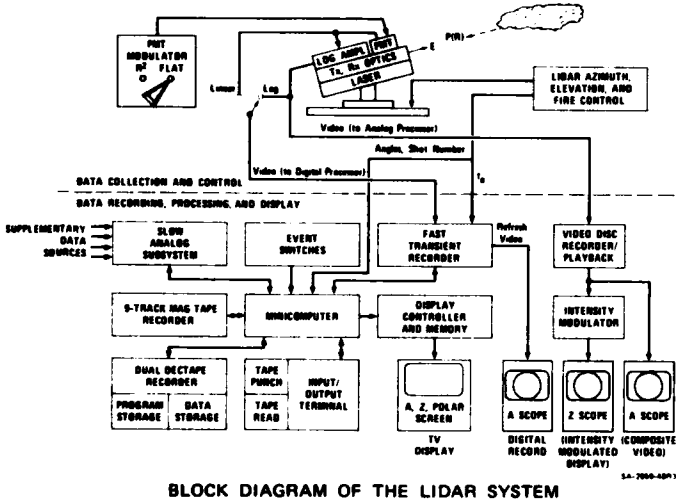

BLOCK DIAGRAM OF THE LIDAR SYSTEM

LIDAR SPECIFICATIONS

TRANSMITTER

6943A Wavelength
0.5 mrad Beamwidth
1.0 J Pulse Energy
30 ns Pulse Length
60 ppm Maximum PRF

RECEIVER

6 inch Newtonian
1 to 5 mrad Field of View
5A Predetection Filter
RCA 7265 PMT Detector
4-decade, 35-MHz Logarithmic Amplifier. Inverse-range-squared or step-function PMT modulation.

DATA SYSTEMS

Analog video disc recording (4.5 MHz) with A-scope and Z-scope real-time displays. Digital magnetic tape (data and programs) recording (25 MHz) with computer processing and real-time TV display (512 x 256 x 4 bit) of processed data.

MOUNT

Automatic azimuth and elevation fire and scan with 0.1° minimum resolution. Automatic reset. Mechanical safety stops.

FIGURE 4 THE SRI MARK IX MOBILE LIDAR SYSTEM

TA-653583-311

Mark IX lidar. The block diagram shown in Figure 5 details the interface connections. The ASL lidar control unit provided the lidar firing rates while interface control signals were developed by a two-lidar interface unit. Basically, an ASL lidar control signal (pre-trigger pulse) was sent to the lidar interface unit located in the Mark IX lidar van; here control signals were generated to prepare the data system to accept ASL lidar backscatter data. When the ASL lidar "fired" it sent a "laser has fired" pulse to the Mark IX transient recorder, and a 10.6-μm (ASL lidar) backscatter record was digitized and recorded on nine-track tape. The lidar interface unit then generated a second set of control signals that prepared the data system to accept a 0.7-μm (Mark IX) backscatter record and also sent a fire pulse to the Mark IX ruby fire-control electronics. When the ruby laser fired, a 0.7-μm backscatter record was digitized and recorded. This sequence of events was repeated for each control signal from the ASL lidar. For the Smoke Week II program the firing rate was set for 1-second intervals.

D. Operating Procedure

The general lidar operating procedure used during the Smoke Week II program was to begin lidar operation prior to an event in order to record a sufficient amount of pre-event data to establish reference conditions for backscatter and transmission analysis. Operation would continue through the event and until backscatter conditions regained the pre-event values, or when lidar operation was stopped for safety reasons. Prior to or following the scheduled events for a day, the Mark IX lidar would perform and record a standard system calibration using calibrated optical attenuators. The Mark IX receiver gain control gates were checked as part of this calibration procedure. The ASL lidar performed a similar calibration but used layers of low-density polyethylene sheets placed in the transmit beam to reduce the received reference signal return. By inserting multiple layers of polyethylene in equal amounts per step, a receiver linearity and dynamic range calibration was made by comparing the changes with calibrated electrical attenuations. The calibration example shown in Figure 6 is a typical calibration recorded on a strip chart. The calibration was also digitally recorded on magnetic tape. The electrical calibration on the left was performed by inserting electrical step attenuators between the receiver detector and post-detector electronics, while the attenuation steps on the right were produced by the transmit beam attenuation method. Since the electrical calibration can be performed very easily, a calibration was generally recorded either before or after each event when the reference signal represented clear-air conditions. Calibration data were used to derive response functions for each lidar (e.g., detector output as a function of light input). Response functions used for the visible and infrared lidar systems are shown in Figure 7. Signature analysis of cloud backscatter and target returns is discussed in Section VI.

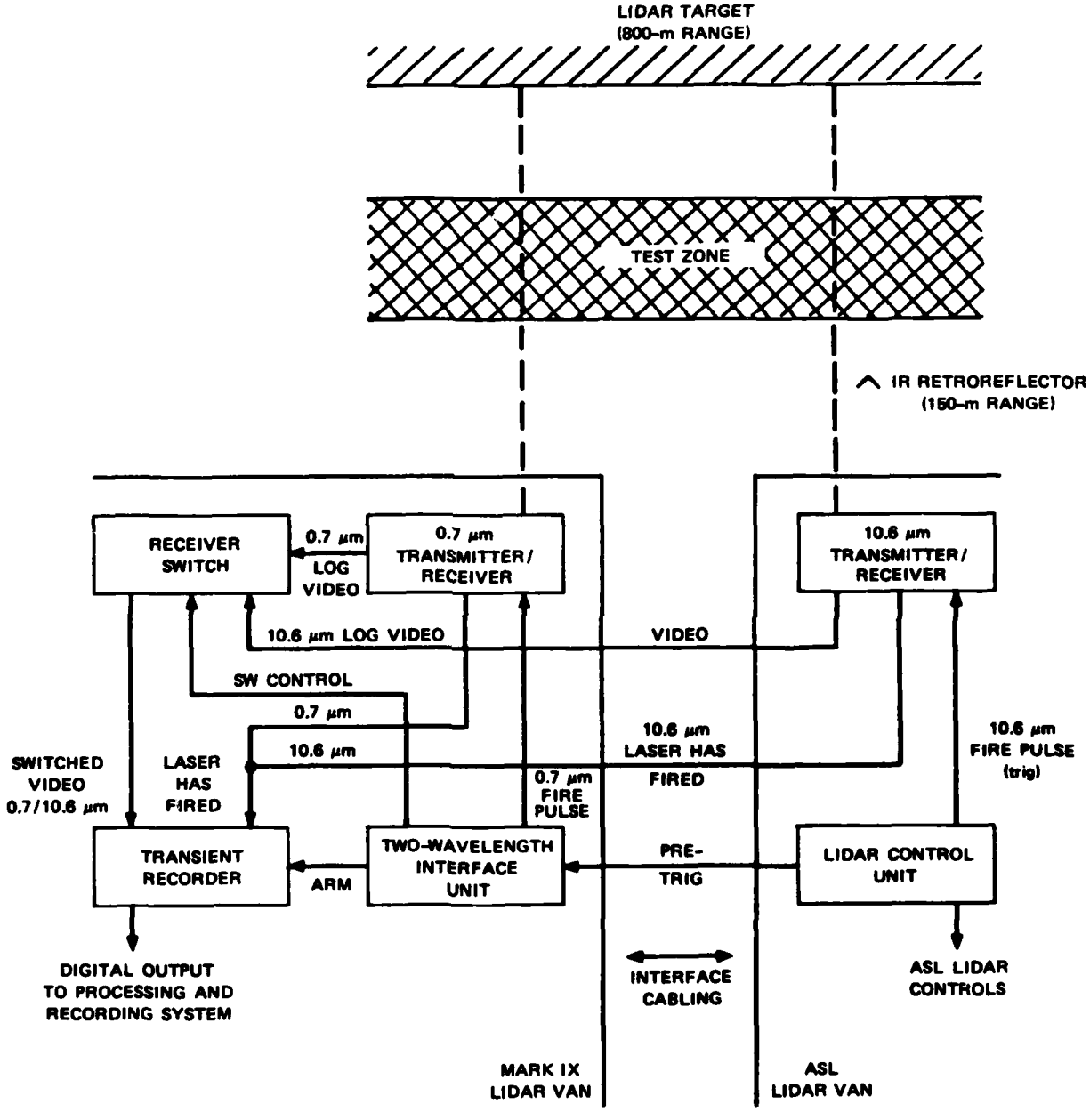

FIGURE 5 TWO-WAVELENGTH INTERFACE BLOCK DIAGRAM

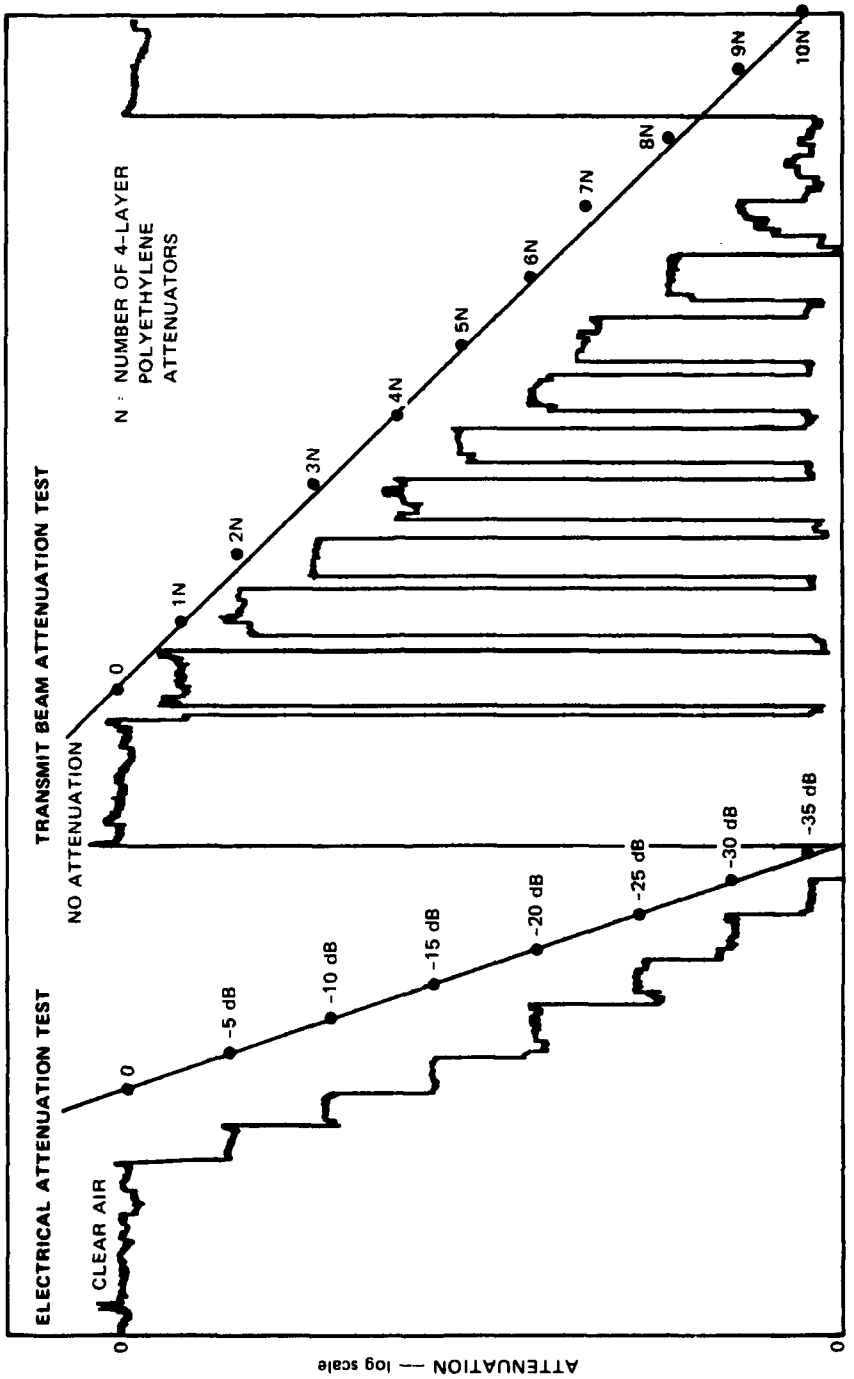

FIGURE 6 ASL LIDAR CALIBRATION DATA

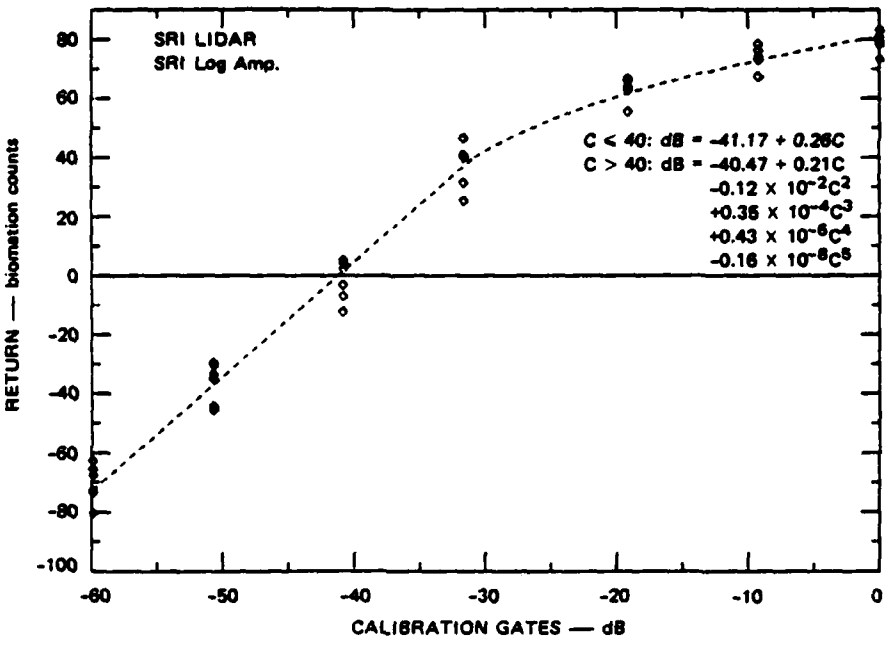

(a) MARK IX LIDAR CALIBRATION

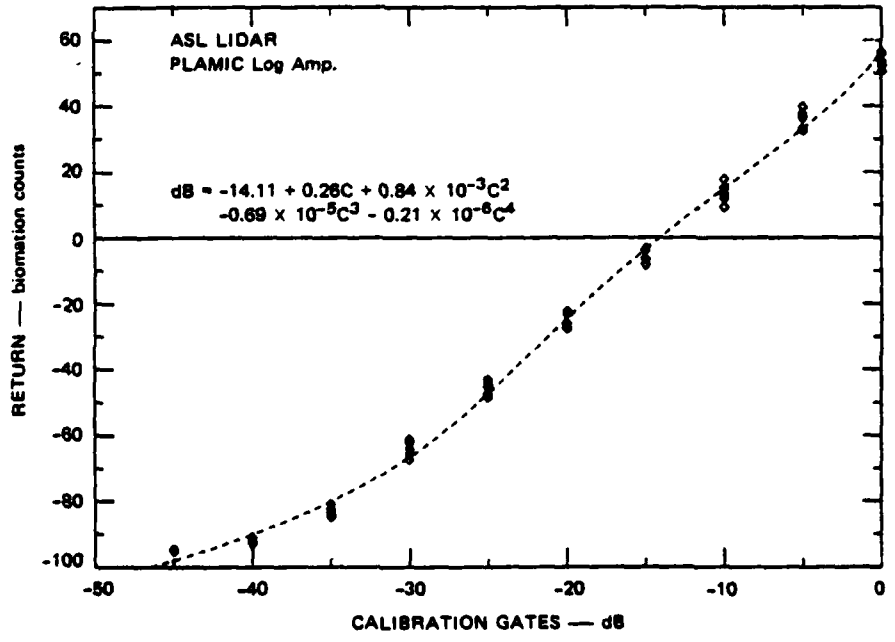

(b) ASL LIDAR CALIBRATION

FIGURE 7 LIDAR CALIBRATION USED FOR ANALYSIS OF SMOKE WEEK II DATA

III EXPERIMENTAL DATA

The two-wavelength ASL/SRI lidar system was used to collect backscatter and transmission data during the Smoke Week II experiments conducted from 6 through 16 November 1978 at Eglin Air Force Base. All observations were made for horizontal paths that nearly coincided with paths viewed by visible and infrared transmissometers operated by the Dugway Proving Ground. Figure 8 presents information on the location of ASL, DPG, and SRI optical sensors as compiled from data presented by Bowman et al. (1979).

Table 2 presents information for the smoke/dust trials observed by the two-wavelength lidar system and discussed in this report. Information on the method of smoke/dust generation is not presented in this report but is discussed in a CONFIDENTIAL report by Bowman et al. (1979).

Backscatter signatures produced by the SRI lidar (0.7-μm wavelength) and the ASL lidar (10.6-μm wavelength) were digitized and written on nine-track magnetic tapes using the digital data system of the SRI lidar. These digital records and the lidar calibration data (Figure 7) form the basis for producing the experimental results presented in the following sections of this report.

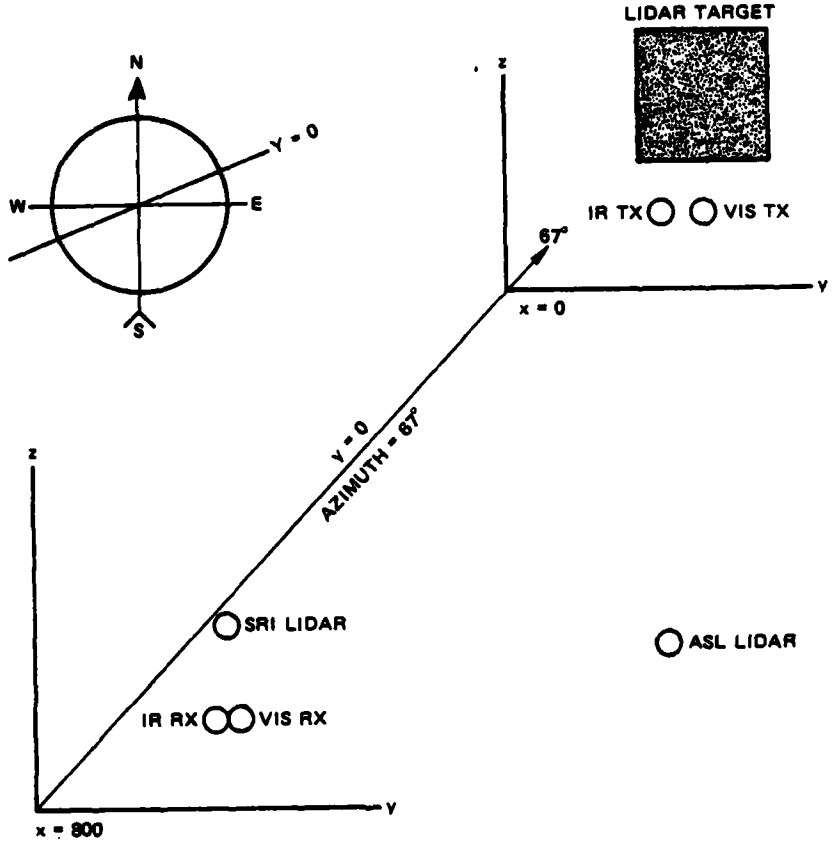

ITEM	x	y	z
ASL lidar	808.09	-14.91	3.99
SRI lidar	808.40	-4.53	4.23
Lidar target	0.00	-3.49	3.76
ASL reflector	657.67	-11.46	2.46
DPG visible transmitter	3.04	-4.64	1.84
DPG visible receiver	804.39	-4.96	2.13
DPG 9.75 μm transmitter	3.05	-3.59	1.93
DPG 9.75 μm receiver	804.37	-4.38	2.13

FIGURE 8 LOCATION OF ASL, DPG, AND SRI LIDAR AND TRANSMISSOMETER INSTRUMENTATION DURING SMOKE WEEK II

Table 2

SMOKE WEEK II EVENTS OBSERVED
BY THE TWO-WAVELENGTH LIDAR SYSTEM
(NOVEMBER 1978)

Trial	Date	Time	Type
1	6	0945	HC
3*	6	1228	P
22*	6	1541	VEH
2*	8	0905	P
6*	8	1204	Ex
4*	8	1322	Ex
5*	8	1428	Ex
11	9	1422	Ex
12	10	0930	Ex
8B	10	1354	P
7*	10	1505	P
9	10	1626	WP
10	11	1105	Ex
13*	11	1231	P
23*	11	1401	HE
14	13	0914	HULK
17*	13	1315	HC
15	13	1418	P
18	14	0947	P
19	14	1117	P
20*	14	1307	P
30	14	1453	HE
23R*	15	0931	HE
21R*	15	1004	Fog oil
24*	15	1059	P
27*	15	1246	VEH
26*	15	1505	HE
25	15	1600	HULK
28	16	1003	P
29	16	1124	HE

Ex = Experimental, VEH = Vehicle dust,
HE = High explosive dust, P = Phosphorus
HULK = Burning vehicle hulk, WP = White phosphorus

*Trial selected for analysis in this study.

IV AEROSOL DISTRIBUTIONS

Using the SRI Mark IX lidar data system, the nine-track magnetic tape records of two-wavelength lidar signatures were processed for range/time intensity-modulated TV displays depicting aerosol distributions along the lidar-to-target path. Results for each trial (Table 2) are presented in Figure 9. The infrared data are displayed below the visible data and features such as target, reflector (IR only), and aerosol cloud returns are indicated. Picture brightness is proportional to the logarithm of lidar observed light intensity.

Range-gated attenuating filters were available on the visible lidar and these were sometimes used to avoid saturation of target and dense aerosol cloud returns. This explains rapid changes in target brightness apparent in Figure 9.

The presentations shown in Figure 9 provide quantitative information on cloud location and dimension along the instrumented path (Figure 2) as a function of time after cloud generation. On several occasions, interference dust resulting from tank operations near the target was observed along the instrumented path, e.g., Trials 1, 14, and 23. Backscatter from the clear air was generally observed at 0.7-μm but not at 10.6-μm.* The picture displays generally indicate equivalence between cloud backscatter observed at 0.7- and 10.6-μm wavelengths. The backscatter generally appears greater at the 0.7-μm wavelength although several trials produced greater backscatter at the 10.6-μm wavelength, e.g., Trials 12, 10, 23, 30, and 29. Visible energy can be greatly attenuated by the cloud while the infrared attenuation may be somewhat less, so that cloud structure observed by the two lidar systems can be different as shown by Figure 9 for Trials 17 and 19. The brightness of the target return (accounting for attenuating filters) provides a qualitative indication of attenuation of the laser energy by the cloud. Larger backscatter seems to be associated with greater attenuation at 0.7 μm, but this correlation is not as evident at 10.6 μm.

The qualitative relationships apparent from Figure 9 encourage further investigation to derive quantitative relationships between backscatter and attenuation. Such relationships may provide the means of readily making transmission measurements along a variety of nonhorizontal paths through the cloud using single-ended lidar techniques.

---

*The 10.6-μm lidar detector was damaged prior to the first trial and was operating at about 15 dB reduction in sensitivity. Clear-air returns were observed with the 10.6-μm ASL lidar during the DIRT-1 tests (van der Laan, 1979).

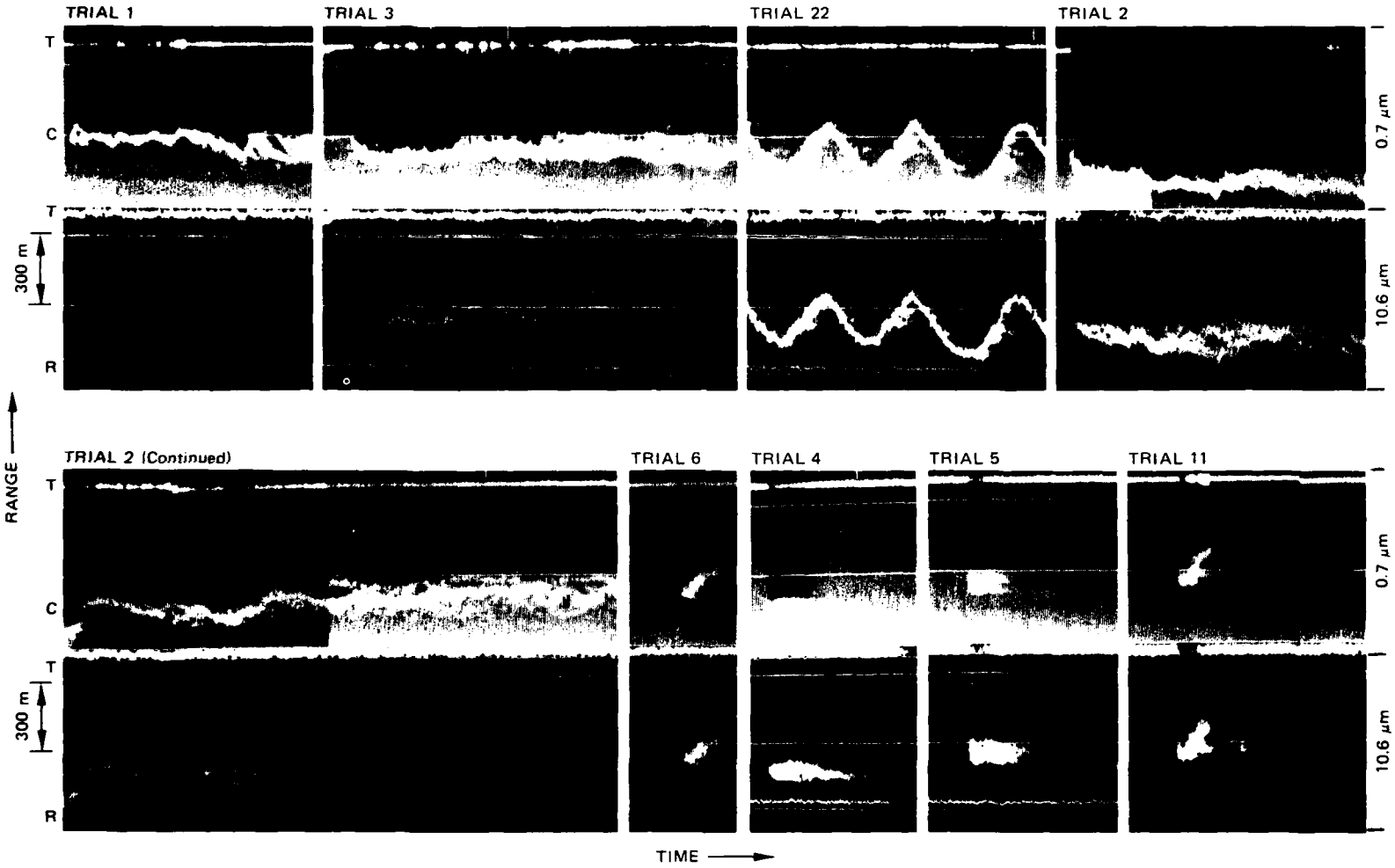

FIGURE 9 RANGE/TIME INTENSITY-MODULATED DISPLAYS DEPICTING LIDAR-OBSERVED STRUCTURE ALONG INSTRUMENTED PATH OF SMOKE WEEK II AEROSOL CLOUDS

Upper record is SRI 0.7-μm wavelength lidar; lower record is ASL 10.6-μm wavelength lidar.
T = Target; C = Cloud; R = Retroreflector (IR only).

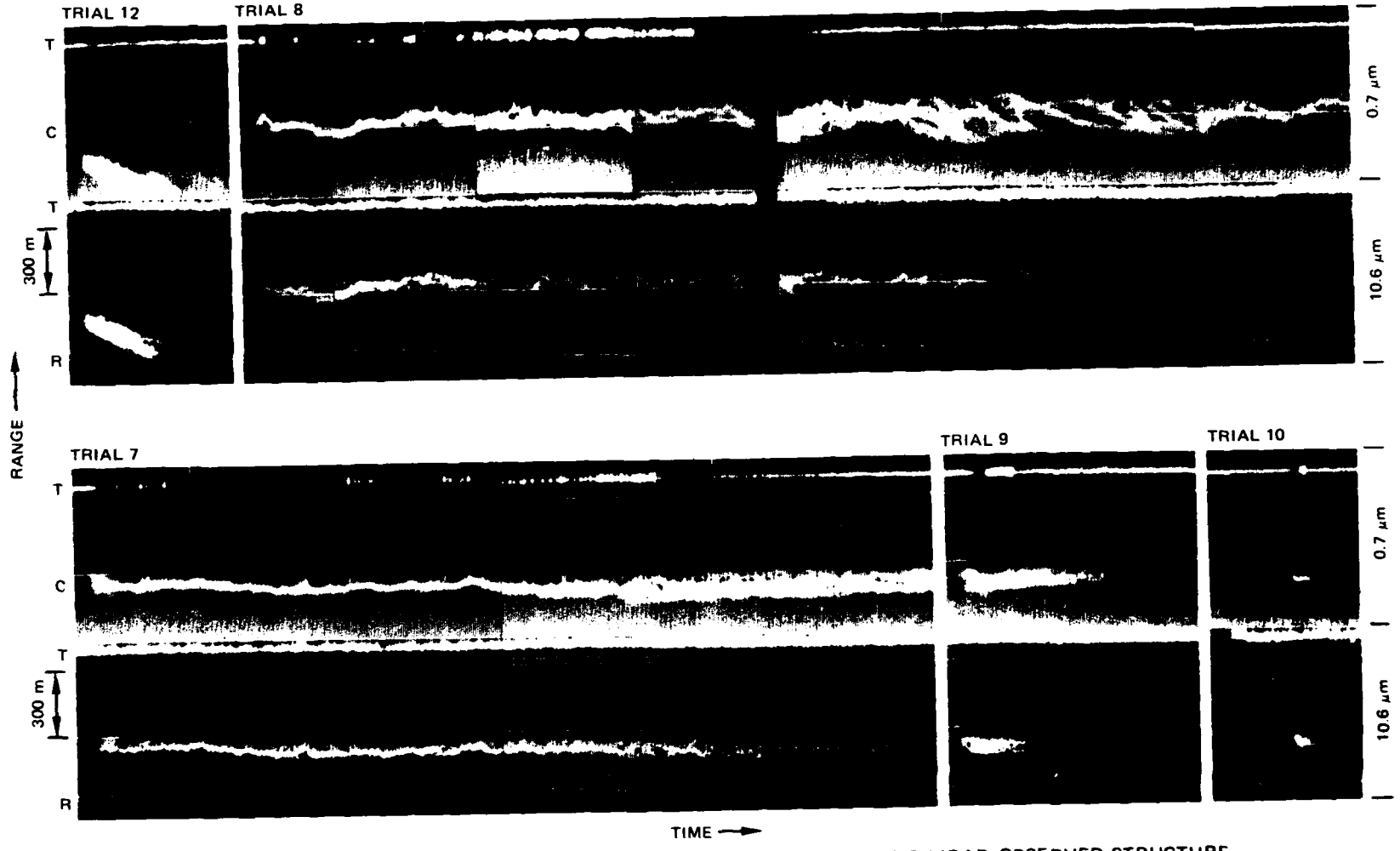

FIGURE 9 RANGE/TIME INTENSITY-MODULATED DISPLAYS DEPICTING LIDAR-OBSERVED STRUCTURE ALONG INSTRUMENTED PATH OF SMOKE WEEK II AEROSOL CLOUDS (Continued)

Upper record is SRI 0.7-μm wavelength lidar; lower record is ASL 10.6-μm wavelength lidar.
T = Target; C = Cloud; R = Retroreflector (IR only).

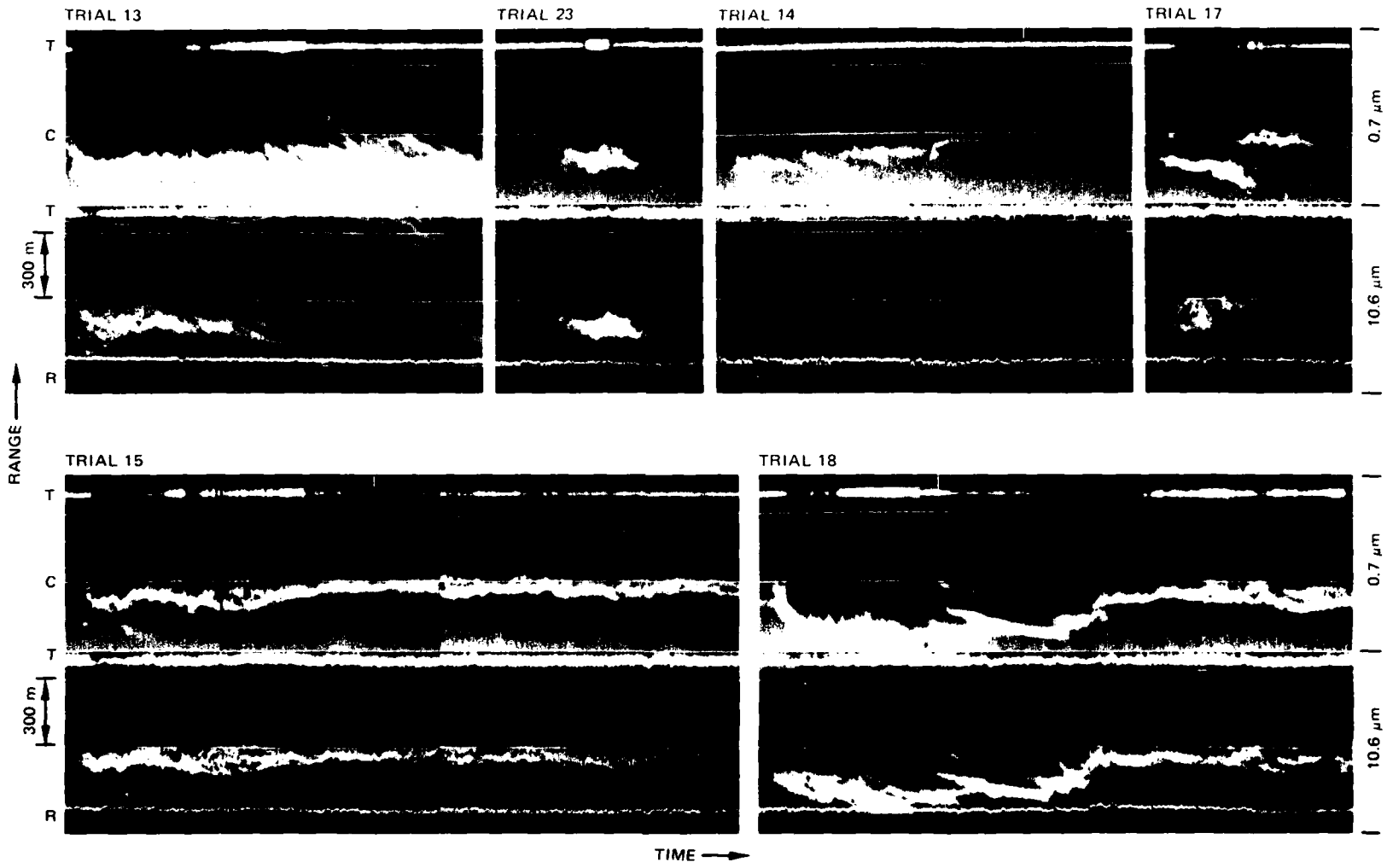

FIGURE 9 RANGE/TIME INTENSITY-MODULATED DISPLAYS DEPICTING LIDAR-OBSERVED STRUCTURE ALONG INSTRUMENTED PATH OF SMOKE WEEK II AEROSOL CLOUDS (Continued)

Upper record is SRI 0.7-μm wavelength lidar; lower record is ASL 10.6-μm wavelength lidar.
T = Target; C = Cloud; R = Retroreflector (IR only).

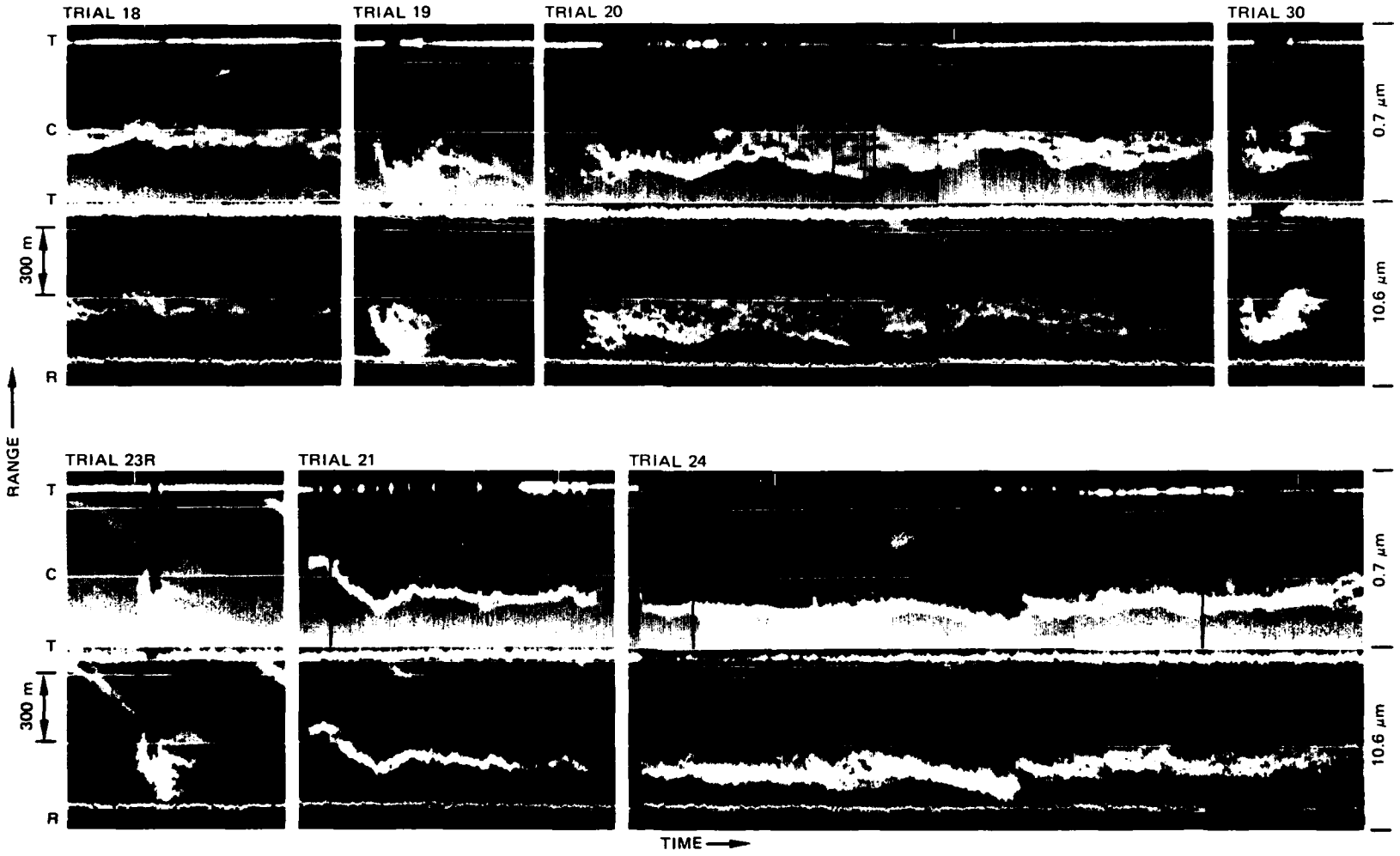

FIGURE 9 RANGE/TIME INTENSITY-MODULATED DISPLAYS DEPICTING LIDAR-OBSERVED STRUCTURE ALONG INSTRUMENTED PATH OF SMOKE WEEK II AEROSOL (Continued)

Upper record is SRI 0.7-μm wavelength lidar; lower record is ASL 10.6-μm wavelength lidar.
T = Target; C = Cloud; R = Retroreflector (IR only).

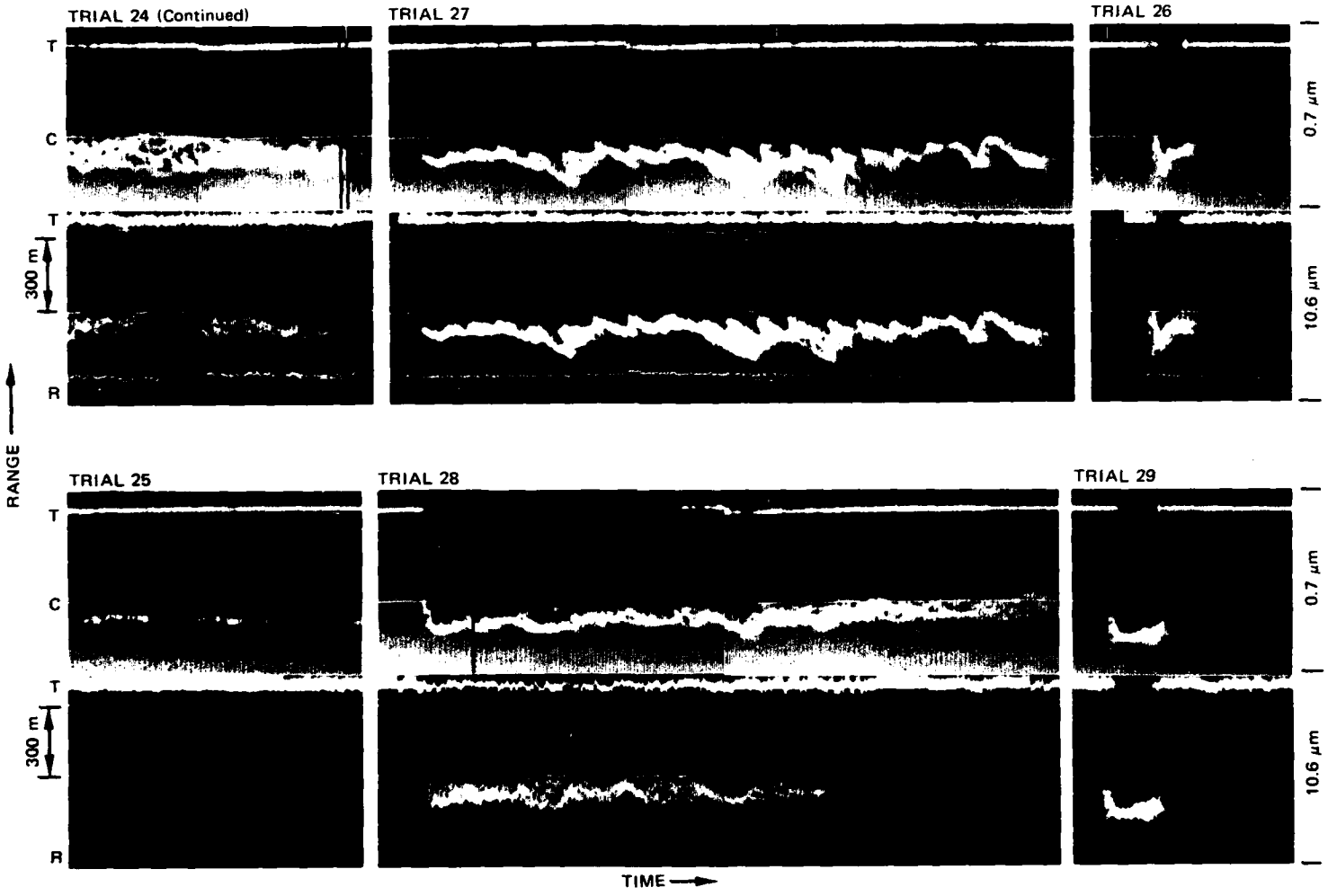

FIGURE 9 RANGE/TIME INTENSITY-MODULATED DISPLAYS DEPICTING LIDAR-OBSERVED STRUCTURE ALONG INSTRUMENTED PATH OF SMOKE WEEK II AEROSOL (Concluded)

Upper record is SRI 0.7-μm wavelength lidar; lower record is ASL 10.6-μm wavelength lidar.
T = Target; C = Cloud; R = Retroreflector (IR only).

Integrated backscatter along the path viewed by the lidar has been shown to be well correlated with transmission for low density aerosols (Uthe, 1978). However, for the high-density aerosol clouds viewed on this project, large attenuation and multiple scattering significantly affect the possibility of deriving transmission data from backscatter measurements. Moreover, the particle size distributions of the aerosol clouds observed at Smoke Week II probably varied greatly with time and space, further adding to the difficulty of deriving cloud density information from the lidar signature data. Nevertheless, lidar provides a promising means of remotely evaluating cloud optical and physical densities, especially in the vertical. This possibility is further investigated in the following sections of this report.

V BACKSCATTER SIGNATURES

The nine-track magnetic tape records of two-wavelength lidar observations made during Smoke Week II were reformatted for analysis by a larger computer system (CDC 6400) located at SRI. Figure 10 illustrates typical lidar waveforms recorded during Trial 7 as produced by the CDC computer plotting facility. The signatures recorded at 60 seconds (s) after the event start time (t_o) are for a relatively dense aerosol cloud as viewed by the visible lidar system. Because of strong attenuation by the cloud, the target return is absent and the backside of the cloud is not observed. Because of less attenuation at the infrared wavelength, the infrared signature shows that the cloud is of greater dimensions than interpreted from the visible signature.

At t_o + 70 s, the target is observed by the visible wavelength system, but the cloud backscatter distribution is very similar to that observed at t_o + 60 s when no target was observed. This is explained by the infrared signature that shows the cloud had smaller dimensions along the path at this time. At t_o + 80 s, a larger target return is seen by the visible system, although a greater cloud return is observed. Clearly, for dense clouds a nonlinear (and probably nonunique) relation exists between path-integrated backscatter and transmission at the visible wavelength. This again is obvious from the backscatter signatures recorded near t_o + 12 min (Figure 10b).

At t_o + 17 min (Figure 10c), the cloud was of relatively low density, as indicated by the little backscatter from the cloud observed by the infrared system and clear air returns observed on the backside of the cloud by the visible system. In this case, the transmission of the cloud in the visible can be computed from the clear-air returns before and after the cloud return. Although relatively high transmissions occur, the area under the cloud return in the visible appears greater than for the dense cloud cases (e.g., at t_o + 60 s). This data example clearly illustrates the usefulness of two-wavelength data for interpretation of lidar signatures.

Earlier results (Uthe, 1978) indicated that the visible lidar system was more sensitive than the infrared lidar system to smoke clouds, while the infrared system was more sensitive to detection of dust clouds. Transmission reduction was greater at the visible wavelength than at the infrared wavelength for smoke particles, but similar for dust particles. Trial 7 data presented above for a smoke cloud also show visible lidar backscatter and transmission are more affected by the cloud than the infrared quantities and are consistent with the earlier results.

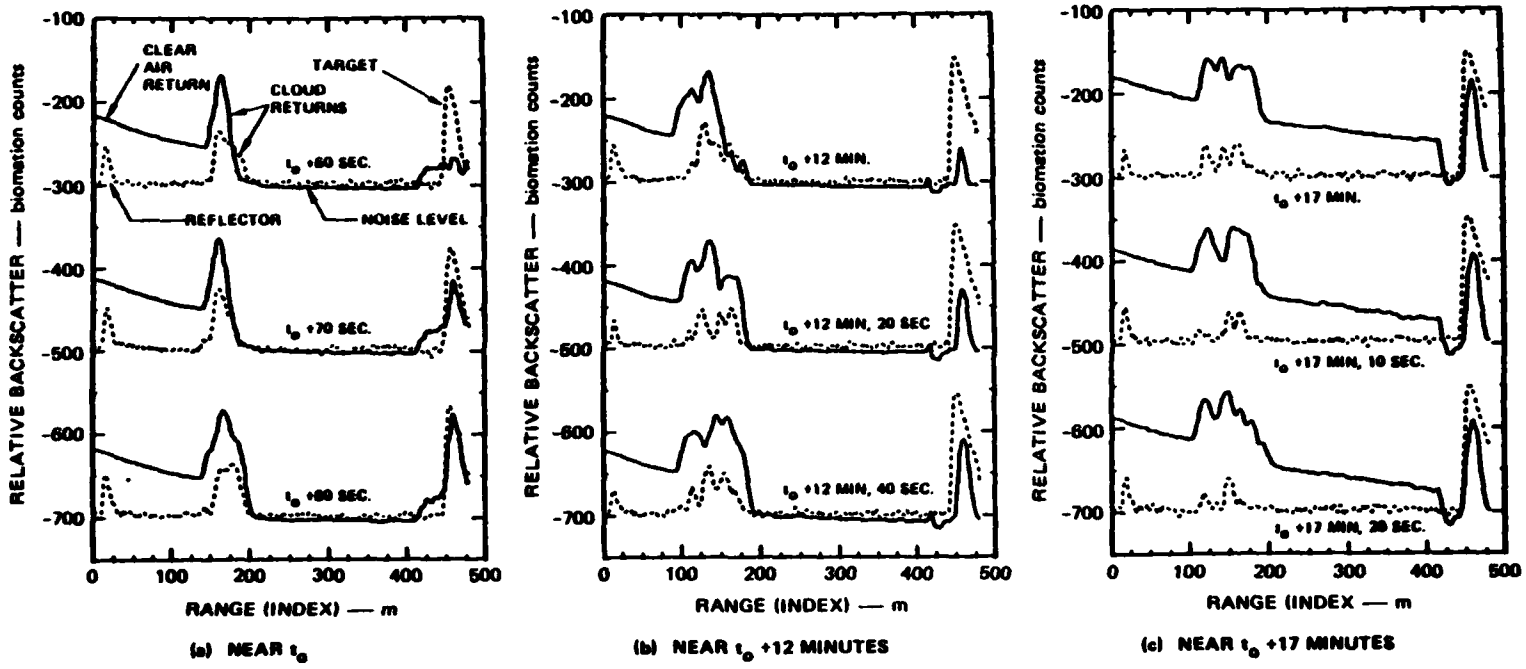

FIGURE 10 VISIBLE AND INFRARED BACKSCATTER SIGNATURES FROM TRIAL 7 OF SMOKE WEEK II

Solid line is visible (0.7 μm); dotted line is infrared (10.6 μm).

The backscatter signatures presented in Figure 11 were recorded during a vehicular dust experiment (Trial 27). The dust-to-clear-air backscatter ratio is greater at the infrared rather than at the visible wavelength. This results primarily because of the low clear-air backscatter at infrared wavelengths. In addition, the dust cloud causes about equal reduction of the visible and infrared target returns, indicating nearly equal transmissions at the two wavelengths, again consistent with earlier reported results. These results show that multiple-wavelength lidar observations can provide some information on the type of aerosol cloud observed.

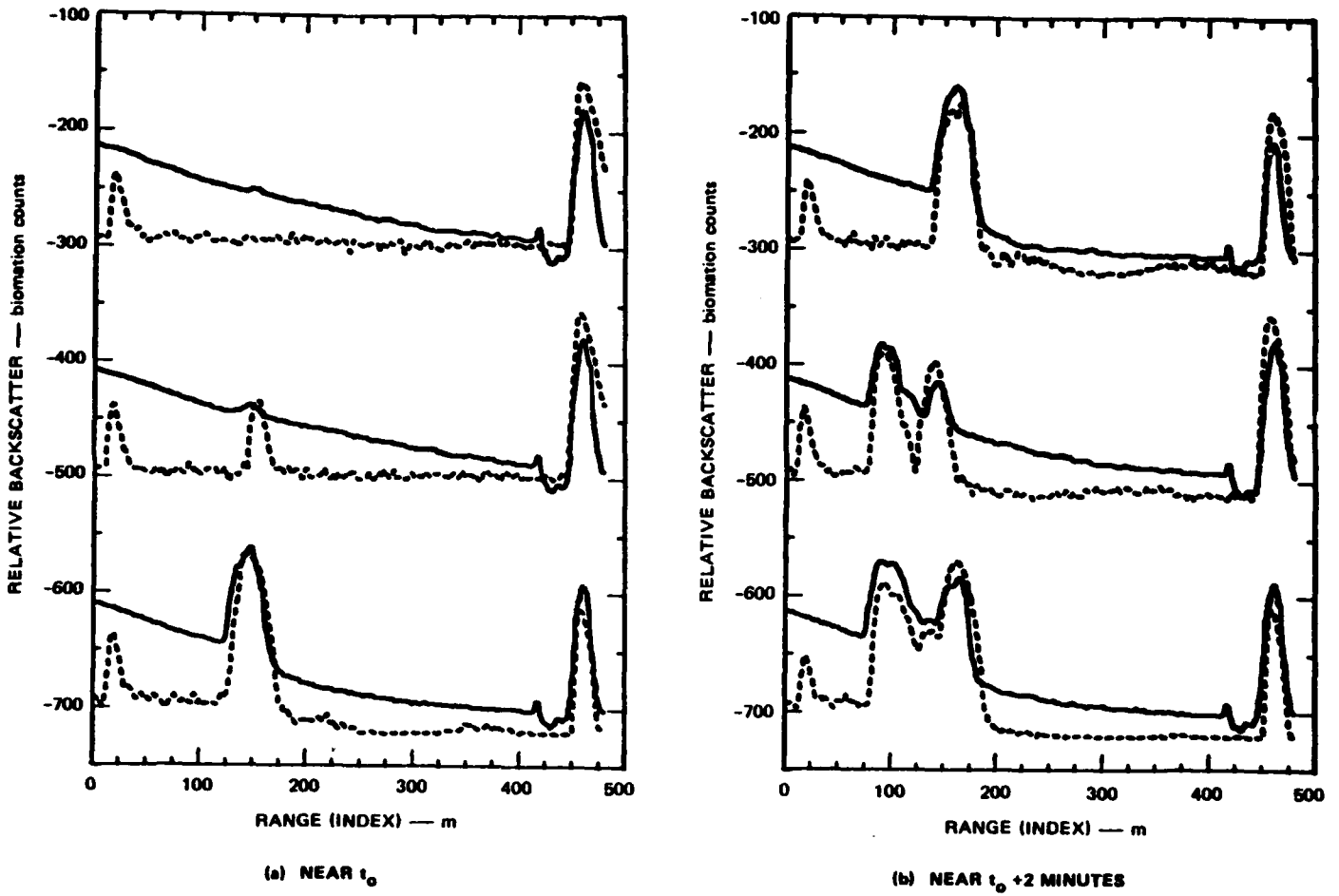

FIGURE 11 VISIBLE AND INFRARED BACKSCATTER SIGNATURES RECORDED DURING TRIAL 27 OF SMOKE WEEK II (VEHICULAR DUST EXPERIMENT)

Solid line is visible (0.7 μm); dotted line is infrared (10.6 μm).

VI SIGNATURE ANALYSIS APPROACH

The objective of this research project was to explore lidar techniques for the remote quantitative evaluation of dense aerosol clouds. The qualitative results presented in the earlier sections of this report indicate that relationships may exist between path-integrated backscatter and transmission of laser energy through the cloud. However, it was also shown that for dense aerosol clouds the path-integrated backscatter may not be uniquely related to transmission--especially at the visible wavelength where attenuation and multiple scattering effects are the greatest. Also indicated was that lidar operation at more than one wavelength should provide improved information on cloud densities over that derived from single-wavelength lidar.

Previous results indicated that the magnitude of the target return observed by the lidar is an excellent indication of transmission of the laser pulse along the path from the lidar to the target (Uthe, 1978). At Smoke Week II, the lidar observation paths were near but did not coincide with the Dugway transmissometer paths as shown in Figure 8. Because of large spatial and temporal variability of the generated particulate clouds, transmissions derived by the lidars and the transmissometers cannot be expected to be equal at all times. Therefore, exploration of relationships between lidar-observed backscatter from the cloud and transmission is best accomplished by using lidar-derived transmissions, providing that valid transmissions can be derived from the lidar signature. The first objective of this study was to demonstrate that transmissions derived from lidar-observed target returns are in agreement with transmissions derived by the Dugway two-ended transmissometers. The second objective was to use the lidar-derived transmissions to determine relationships between lidar-observed backscatter from dense aerosol clouds and transmission through the clouds, and in turn to develop a technique for estimating transmission over slant and vertical paths through dense clouds in future experiments.

Sixteen Smoke Week II trials were selected for signature analysis on the basis of data quality as indicated by the gray-scale presentations of Figure 9. The sixteen trials selected for analysis are indicated in Table 2. The backscatter signatures for these trials were corrected for receiver nonlinearities (Figure 7) and resulting logrithmic values of light input were corrected for the inverse-range squared factor and linearized for further processing in terms of transmission and integrated backscatter.

For each trial selected for analysis, the transmission as a function of time relative to the start of the smoke/dust event (t_o) was computed from the lidar-observed target returns. Transmissions were computed at both 0.7- and 10.6-μm wavelengths using the relations:

$$T_t = (R_t/R_{to})^{\frac{1}{2}}$$

where

T_t = transmission at time t,

R_t = target return (linear form),

R_{t_o} = target return during "clear-air" conditions.

Visible and infrared transmissometer data presented in graphical form by Dugway Proving Ground (Gooley and Smallers, 1978) were digitized using a curve-following technique. The lidar and transmissometer transmission values were used to generate the following data plots:

(a) Lidar-derived transmissions at 0.7- and 10.6-μm wavelengths as a function of time relative to the start of the smoke/dust event.

(b) Lidar- and transmissometer-derived transmissions at 0.7-μm wavelength as a function of time relative to the start of the smoke/dust event.

(c) Lidar- and transmissometer-derived transmissions at 10.6-μm wavelength as a function of time relative to the start of the smoke/dust event.

The lidar backscatter signatures were corrected for receiver response using the relationships shown in Figure 7. Resulting signatures were corrected for the inverse-range-squared factor and normalized to signal levels observed before the laser pulse entered the particulate cloud:

$$S(R) = 10 \log_{10} \frac{P(R)R^2}{P_o R_o^2} ,$$

where P_o is the clear-air lidar return at range R_o on the near side of the cloud return. The signature values were then linearized by the expression

$$S_L = 10^{S/10} - 1 ,$$

and then path-integrated over the range interval for which cloud returns were observed

$$B = \int_{\text{cloud}} S_L(R)\,dR .$$

These path-integrated backscatter values B and the lidar-derived optical depths u = -ln T were plotted in the following manner:

(d) Integrated normalized backscatter at 0.7- and 10.6-μm wavelengths as a function of time relative to the start of the smoke/dust event.

(e) Optical depth at a wavelength of 0.7-μm as a function of integrated normalized backscatter at a wavelength of 0.7 μm.

(f) Optical depth at a wavelength of 10.6-μm as a function of integrated normalized backscatter at a wavelength of 10.6 μm.

(g) Optical depth at a wavelength of 0.7-μm as a function of integrated normalized backscatter at a wavelength of 10.6 μm.

The data plots (a) through (g) for each of the sixteen Smoke Week II trials chosen for analysis are presented and discussed in the following section.

VII SIGNATURE ANALYSIS RESULTS

The type of data plots discussed in the previous section of this report are presented below for sixteen Smoke Week II trials. Information on wind direction and speed and on particle size distribution as measured by Dugway Proving Ground (Gooley and Smalley, 1978) and mean particle size measured by the University of Tennessee Space Institute (Farmer et al., 1979) is presented in Table 3 for relating to the lidar and transmissometer optical measurements. However, as shown by Table 3, significant differences exist between the particle size results obtained by the two measurement groups. Also, movement of smoke/dust clouds was observed to deviate from that expected by the mean wind direction (Smith and Shih, 1979) so that these supplementary data are of only limited use in the interpretation of the lidar results.

Table 3

WIND AND PARTICLE SIZE INFORMATION FROM DUGWAY PROVING GROUND
AND MEAN PARTICLE SIZE FROM UNIVERSITY OF TENNESSEE SPACE INSTITUTE (UTSI)

Trial	Type	Wind		Particle Size (Dugway) Percent in Indicated Size Range--um						Mean Diameter (UTSI) um
		Speed (mps)	Direction (deg)	0.3-0.4	0.4-0.6	0.6-0.8	0.8-1.0	1.0-1.5	1.5-3.0	
2	P	4.3	358	18	19	18	8	21	16	1.85
3	P	3.7	163	23	22	22	13	16	16	--
				24	25	18	12	17	4	--
4	Ex	--	--	--	--	--	--	--	--	--
5	Ex	--	--	--	--	--	--	--	--	3.8
6	Ex	--	--	--	--	--	--	--	--	1.2
7	P	2.9	150	49	34	11	3	2	0	--
				19	19	21	41	19	7	--
13	P	3.1	38	53	35	9	2	1	0	--
				56	32	8	2	1	0	--
17	HC	3.2	141	29	26	20	10	12	3	--
				17	21	16	11	19	17	--
20	P	2.5	150	--	--	--	--	--	--	--
21R	Oil fog	3.8	134	11	13	17	13	25	20	2.38
				9	16	17	14	30	14	--
22	VEH	4.4	142	13	6	74	4	1	1	13.8
				38	17	41	4	0	0	--
23	HE	3.3	007	2	48	47	1	0	2	15.7
				--	--	--	--	--	--	--
23R	HE	3.0	109	55	20	23	1	0	1	12.7
				34	23	30	13	0	0	--
24	P	4.0	126	32	27	19	9	11	1	--
				28	27	17	10	14	4	--
26	HE	4.0	178	43	23	32	1	0	0	11.32
				25	26	46	1	0	0	--
27	VEH	3.6	114	43	14	39	4	0	1	17
				--	--	--	--	--	--	--
30	HE	2.3	170	51	23	25	1	0	0	15.8
				21	21	34	24	0	0	--

Optical measurement path aligned at an azimuth of 67°

Ex = Experimental; VEH = Vehicular dust; HE = High explosives; P = Phosphorus

A. Trial 2

Plots of optical data collected for Trial 2 are presented in Figure 12. This phosphorus cloud greatly reduced transmission of the visible laser pulse over that of the infrared laser pulse as shown in Figure 12a. Larger transmissions were recorded by the lidar systems than the transmissometer systems at both visible (Figure 12b) and infrared (Figure 12c) wavelengths. This may have resulted because of greater smoke concentrations near the surface than at elevated levels, as has been noted by Smith and Shih (1979) for phosphorus trials.

As shown by Figure 9, the cloud drifted near the lidar between t_o + 2 and t_o + 11 min so that sufficient clear-air on the near side of the smoke cloud was not observed to compute normalized backscatter relative to clear air backscatter. The greater extinction and backscatter observed at the visible wavelength over that observed at the infrared wavelength indicates small particle sizes--consistent with the particle size data of UTSI (Table 3).

Optical depths evaluated from the target returns are plotted against integrated backscatter evaluated from the aerosol cloud returns in Figure 12e, 12f, and 12g. These results show a large degree of data scatter, although a linear relationship is indicated between the quantities at 10.6-μm wavelength. As will be shown by other data presented in this section, the poorest correlation between cloud attenuation and cloud backscatter was obtained for the phosphorus and oil fog events.

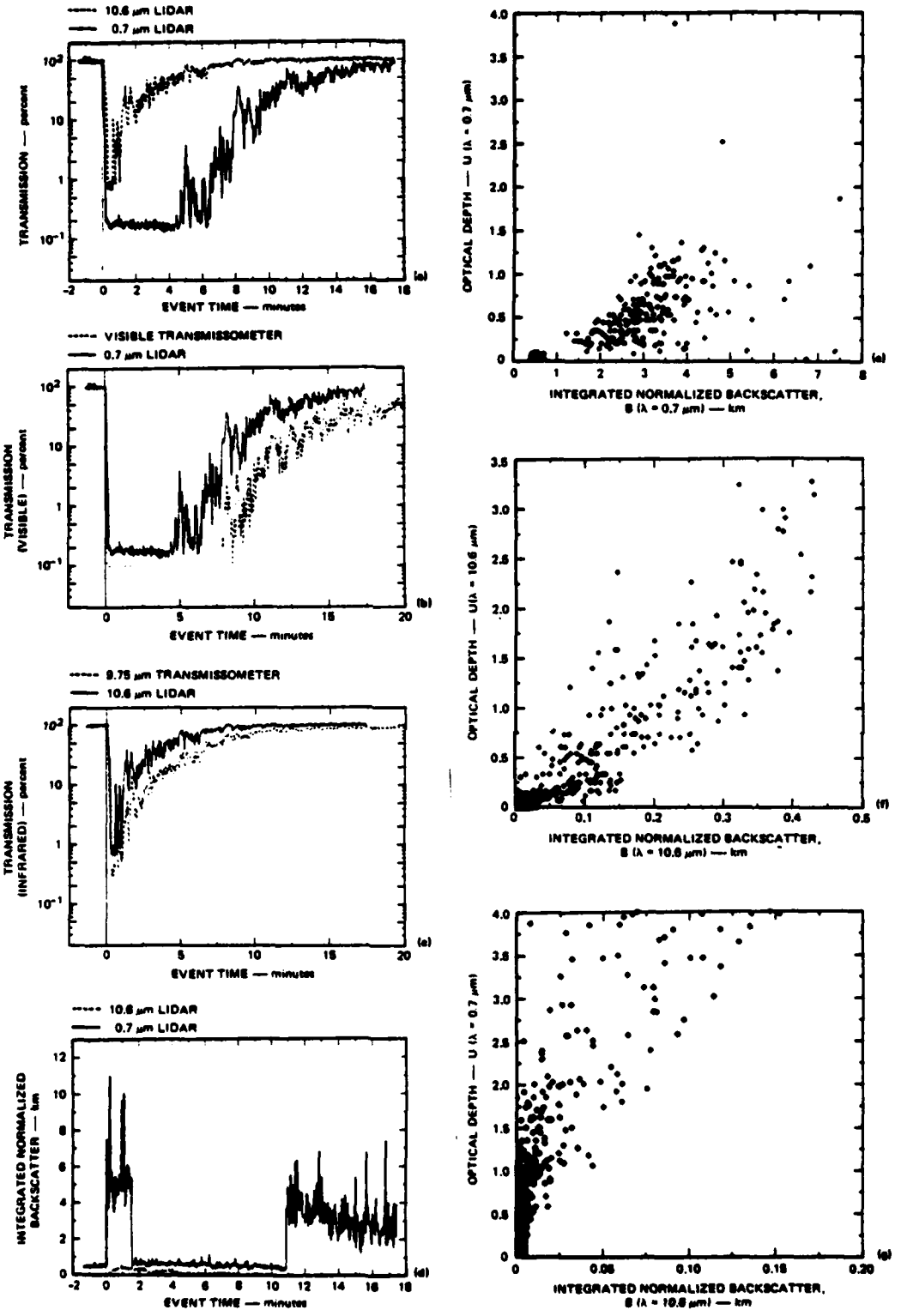

FIGURE 12 ATTENUATION AND BACKSCATTER DATA PLOTS FOR SMOKE WEEK II, TRIAL 2 (PHOSPHORUS)

B. Trial 3

Trial 3 was also a phosphorus event, and as for Trial 2, the cloud attenuated the visible laser pulses significantly more than the infrared laser pulses (Figure 13a). In the visible, the transmissometer data show greater attenuation than the lidar data but not as large a difference as for Trial 2. The lidar and transmissometer attenuation data are in excellent agreement (Figure 13c). Because of the position of the lidar and transmissometer instrumentation (Figure 8), the results of this test indicate that cloud inhomogeneities in the vertical introduce greater differences between lidar and transmissometer records than inhomogeneities in the horizontal direction of cloud travel. As for Trial 2, the normalized backscatter at the visible wavelength is many times greater than in the infrared. Also, a large degree of data scatter is obtained in the plots of optical depth against integrated backscatter. At the visible wavelength, integrated backscatter becomes independent of optical depth for optical depth values greater than about 1.0 (transmission of 37 percent).

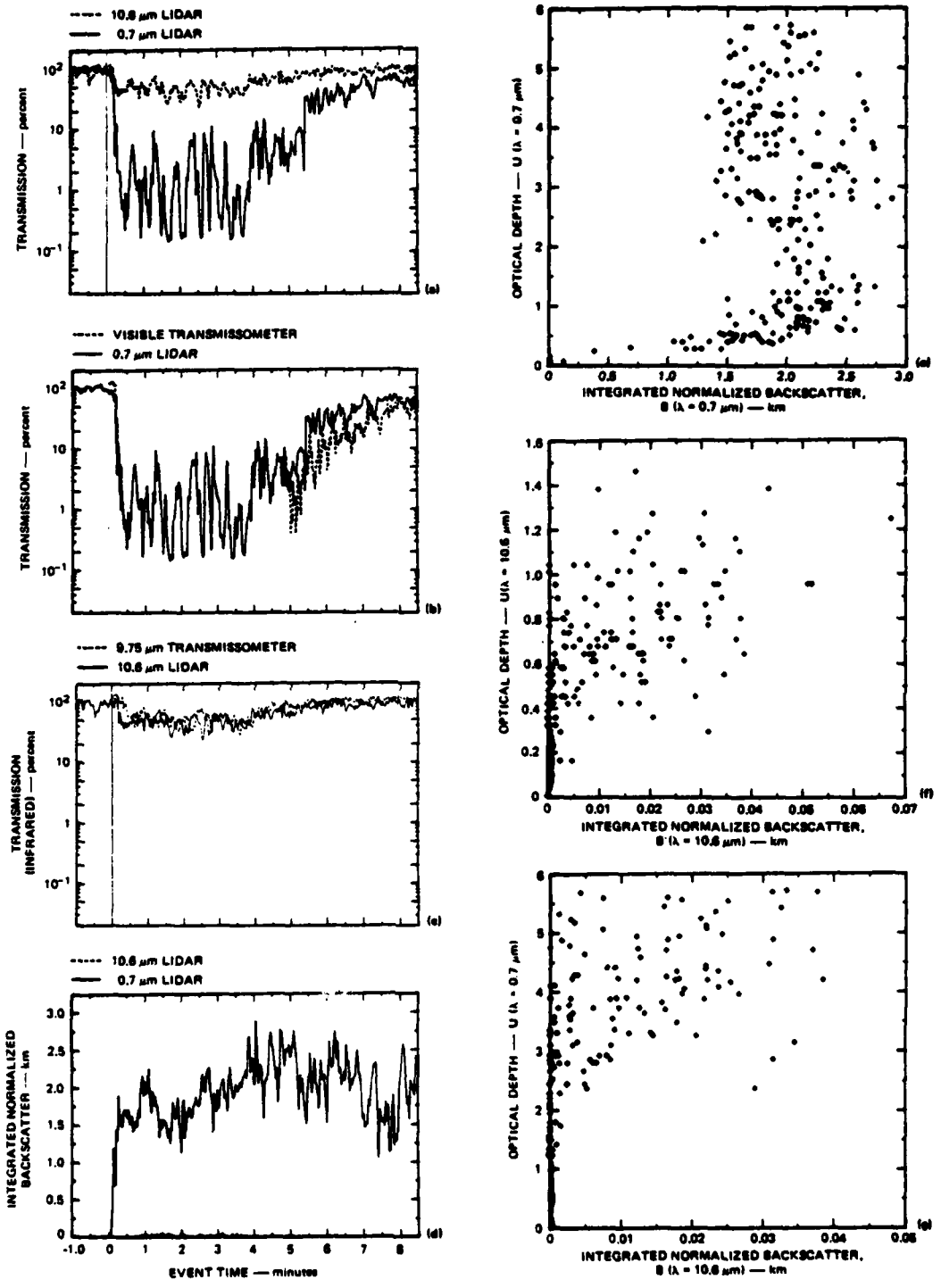

FIGURE 13 TRANSMISSION AND BACKSCATTER DATA PLOTS FOR SMOKE WEEK II, TRIAL 3 (PHOSPHORUS)

C. Trial 4

The lidar and transmissometer attenuation data for Trial 4 (Figure 14) are in good agreement and both indicate that this experimental particle cloud caused slightly more attenuation at the visible wavelength than at the infrared wavelength--possibly indicating relatively small particle sizes. However, unlike the phosphorus clouds of Trials 2 and 3, the cloud backscatter is much greater at the infrared than the visible wavelength, possibly indicating that these particles greatly absorb energy in the visible part of the spectrum.

The relationship between optical depth and backscatter is better defined than for the phosphorus clouds because of less attenuation in this trial. In addition, significantly less data scatter occurs between attenuation and backscatter, possibly indicating that particle sizes were less variable during the observational period than for the phosphorus clouds.

Visible integrated backscatter is a good indicator of visible extinction for optical depths less than about 1.5. Infrared integrated backscatter is an indicator of infrared extinction for optical depths less than about 0.2. In Figure 14g, the two data points above an optical depth of 2.0 are invalid because the cloud was viewed by the visible lidar but not by the infrared lidar. These data points clearly show that cloud inhomogeneities can introduce significant data scatter when comparing Smoke Week II infrared and visible optical terms.

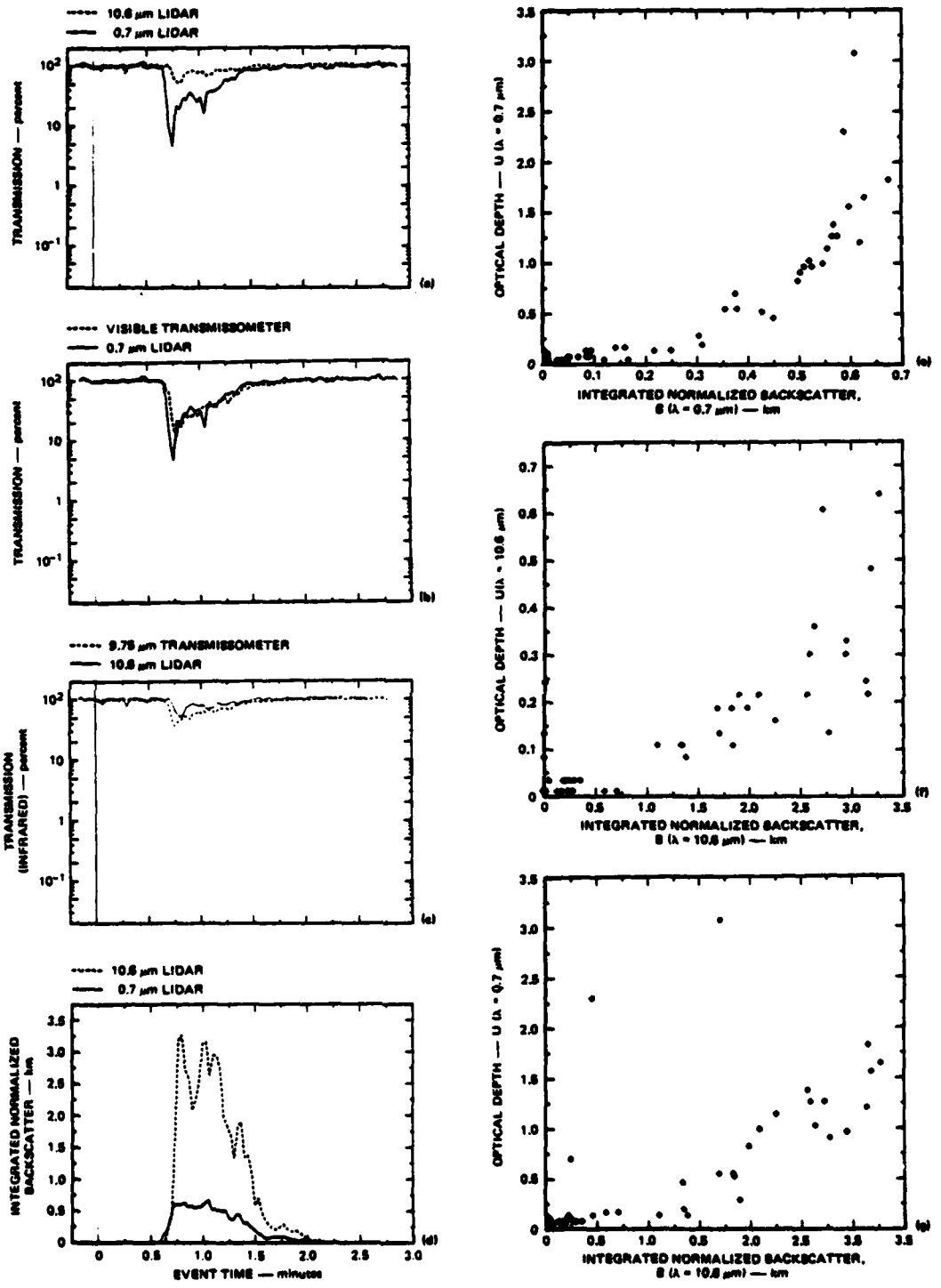

FIGURE 14 TRANSMISSION AND BACKSCATTER DATA PLOTS FOR SMOKE WEEK II, TRIAL 4 (EXPERIMENTAL PARTICLES)

D. Trial 5

Like Trial 4, Trial 5 (Figure 15) was conducted with an experimental particle material. The lidar and transmissometer records agree relatively well and both indicate greater attenuation at the infrared wavelength, although this is not conclusive because of the short time period of the event and the separated optical paths. However, it is clearly evident that this material is also much more reflective in the infrared than the visible (Figure 15d). Integrated backscatter is a relatively good indicator of transmission for optical depths of less than 1.5 in the visible and infrared (Figure 15e and f).

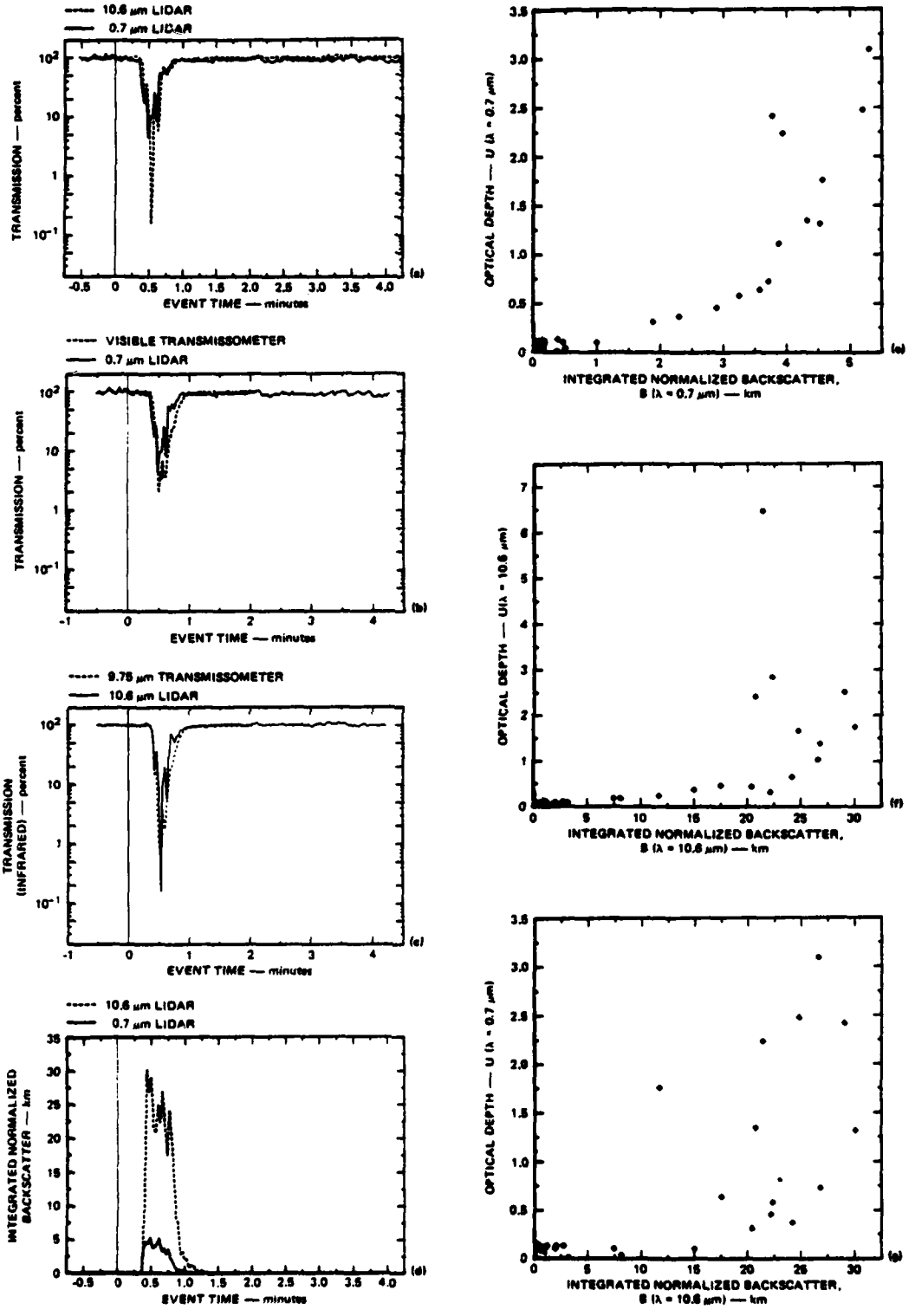

FIGURE 15 TRANSMISSION AND BACKSCATTER DATA PLOTS FOR SMOKE WEEK II TRIAL 5 (EXPERIMENTAL PARTICLES)

E. Trial 6

The experimental particle material used in Trial 6 (Figure 16) produced relatively strong backscatter and weak attenuation at both visible and infrared wavelengths. The integrated backscatter is a good indicator of attenuation at the visible and infrared for the range of aerosol densities observed (Figure 16e and f). Infrared backscatter does not appear to be a better estimator of visible transmission as compared to visible backscatter (Figure 16e and g).

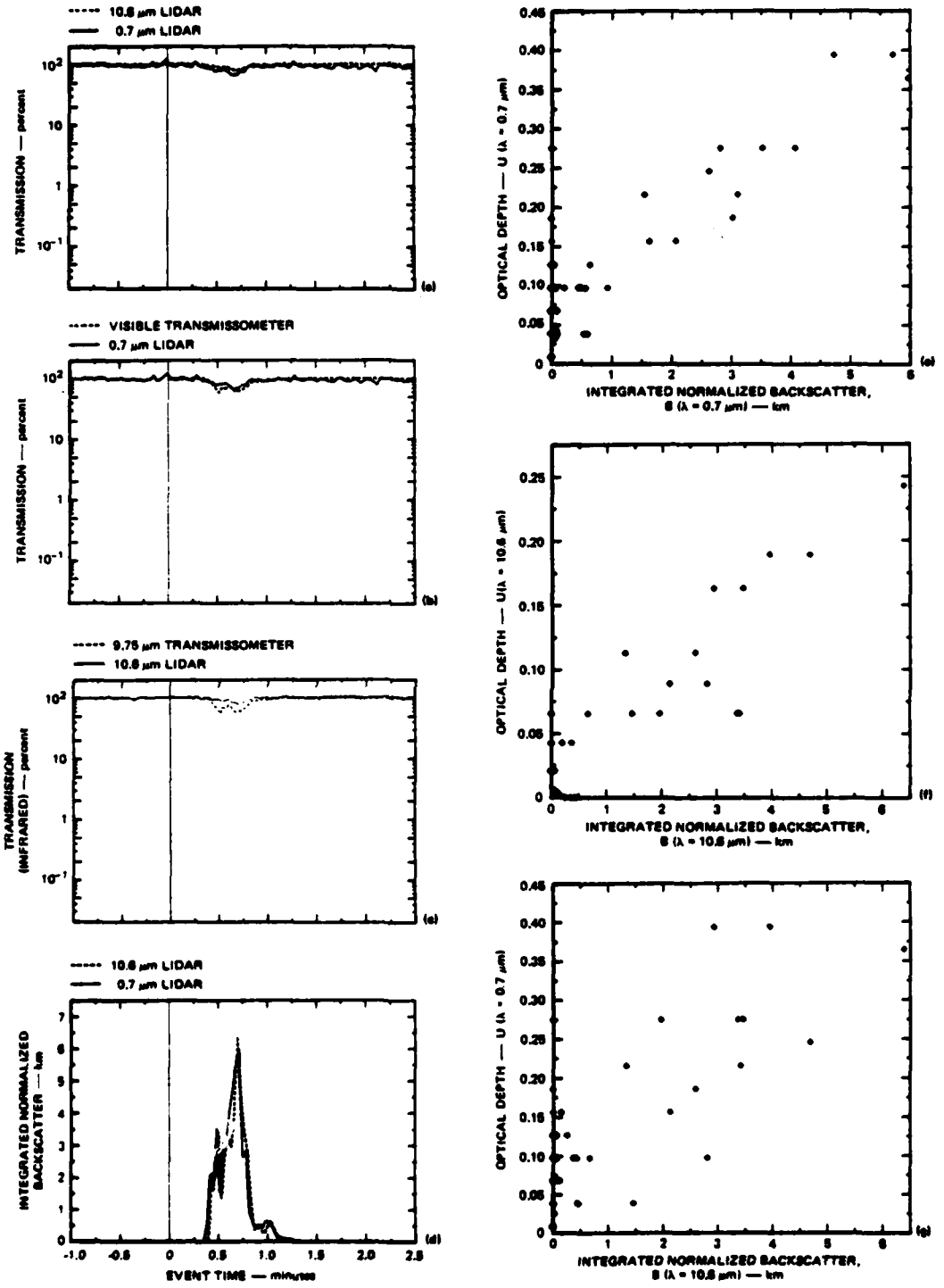

FIGURE 16 TRANSMISSION AND BACKSCATTER DATA PLOTS FOR SMOKE WEEK II, TRIAL 6 (EXPERIMENTAL PARTICLES)

F. Trial 7

Like earlier phosphorus events, Trial 7 resulted in significantly greater attenuation of the visible laser energy than the infrared laser energy (Figure 17a). While substantial differences were obtained between the lidar and transmissometer records in the visible, the data from the two instruments in the infrared are in nearly perfect agreement. Because of the placement of the instruments, this again indicates large spatial differences in cloud density in the vertical direction. As for the other phosphorus events, the cloud backscattered visible energy more effectively than infrared energy (Figure 17d).

The observed values of optical depth plotted against integrated backscatter presented in Figure 17e show a large amount of data scatter, possibly indicating variable particle sizes during the event. A linear relationship between optical depth and integrated backscatter is apparent for optical depths of less than 1.0. For values above 1.0, integrated backscatter actually decreases slightly for increasing values of optical depth. This results because energy returned to the lidar from the far side of the cloud is attenuated by the near-side cloud particles to such an extent that the far side returns are below the noise level of the lidar receiver. Therefore, as cloud density increases the path-integrated backscatter remains nearly constant.

Although a significant amount of data scatter occurs in the plot of infrared optical depth against infrared integrated backscatter, a relationship between these quantities is more linear than in the visible. This is expected because of the greatly reduced attenuation in the infrared. Figure 17g shows that the integrated backscatter at the infrared wavelength is a better indicator of visible optical depth than is the integrated backscatter at the visible wavelength.

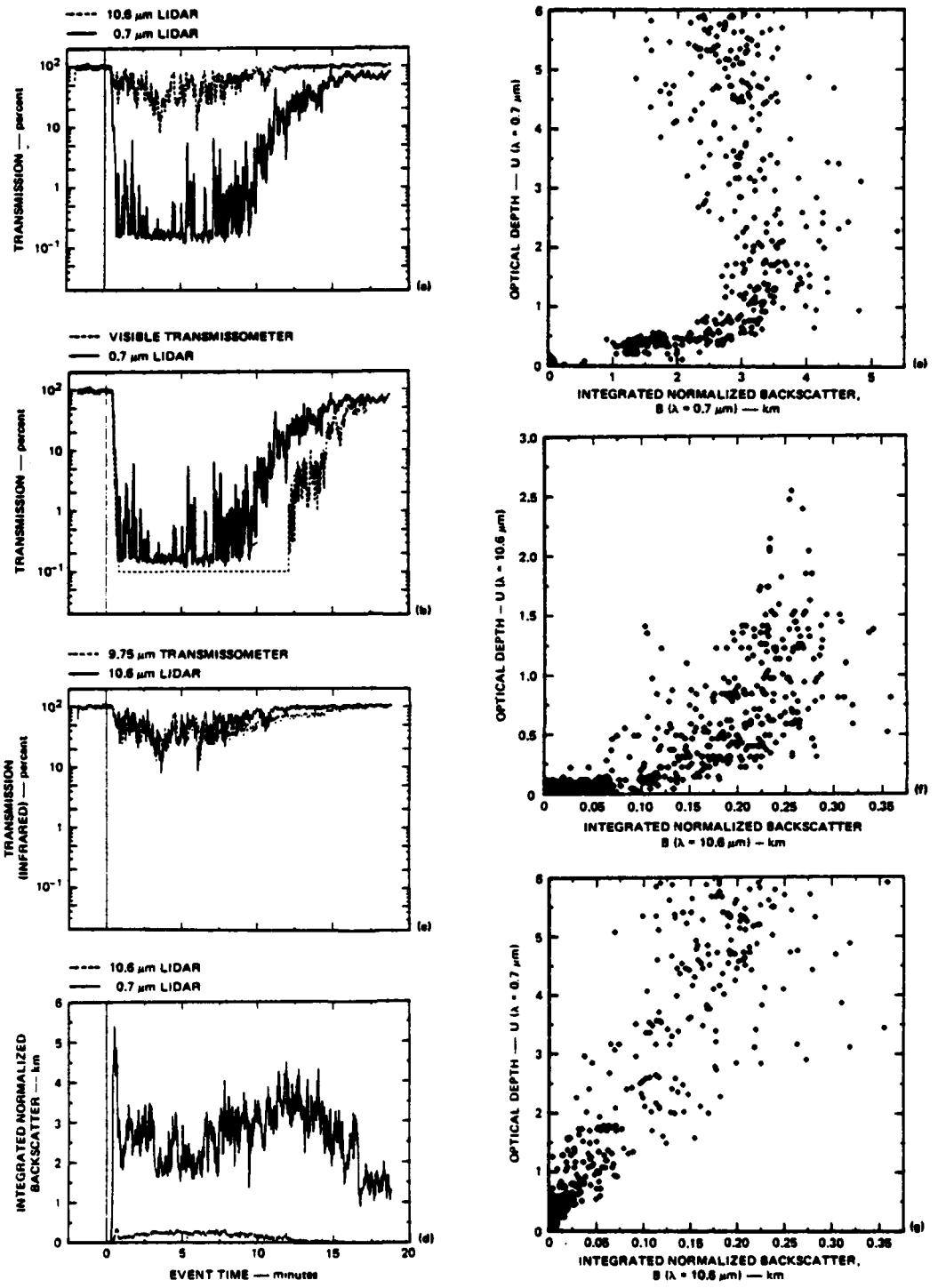

FIGURE 17 TRANSMISSION AND BACKSCATTER DATA PLOTS FOR SMOKE WEEK II, TRIAL 7 (PHOSPHORUS)

G. Trial 13

The comments made about Trial 7 (Figure 17) also pertain to the Trial 13 (Figure 18) phosphorus event. From Figure 18 we concluded that:

(1) Significantly greater attenuation occurs at the visible wavelength than at the infrared wavelength.

(2) Good correspondence between the lidar and transmissometer records is obtained at the infrared wavelength.

(3) Significant differences occur between the visible lidar and transmissometer records.

(4) Much larger backscatter occurs at the visible wavelength.

(5) Large data scatter occurs between observations of optical depth and integrated backscatter.

(6) Integrated backscatter is independent of optical depth at large optical depths.

(7) Integrated backscatter at the infrared is a better indicator of visible optical depth than integrated backscatter at the visible.

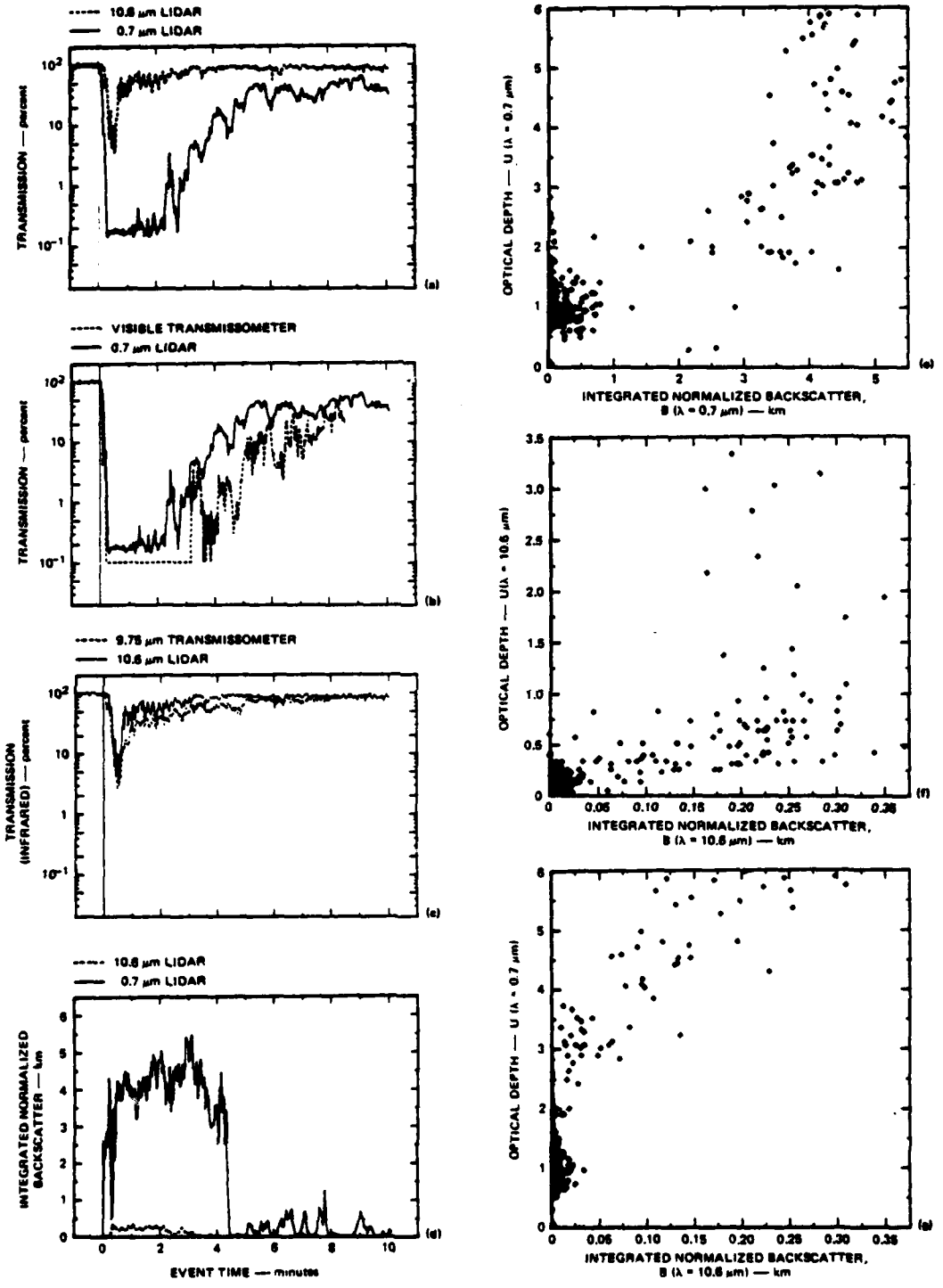

FIGURE 18 TRANSMISSION AND BACKSCATTER DATA PLOTS FOR SMOKE WEEK II, TRIAL 13 (PHOSPHORUS)

H. Trial 17

Trial 17 was an HC ($ZnC\ell_2$ obscurant) event. As for the phosphorus events, attenuation at the visible lidar wavelength greatly exceeds that at the infrared lidar wavelength (Figure 19a). Excellent agreement is obtained between the transmission records for the lidar and transmissometer for both visible (Figure 19b) and infrared (Figure 19c) wavelengths. In addition to showing equivalence of the lidar and transmissometer techniques, these data indicate that the HC cloud was spatially more uniform than the phosphorus clouds. Like the phosphorus events, much greater cloud-to-clear-air backscatter is observed at a wavelength of 0.7 μm than at 10.6 μm. Integrated backscatter is a relatively good indicator of cloud attenuation at the visible wavelength for optical depths of less than 1.0. Very poor correlation is obtained between these quantities in the infrared (10.6 μm), probably because only small attenuation and backscatter occurred.

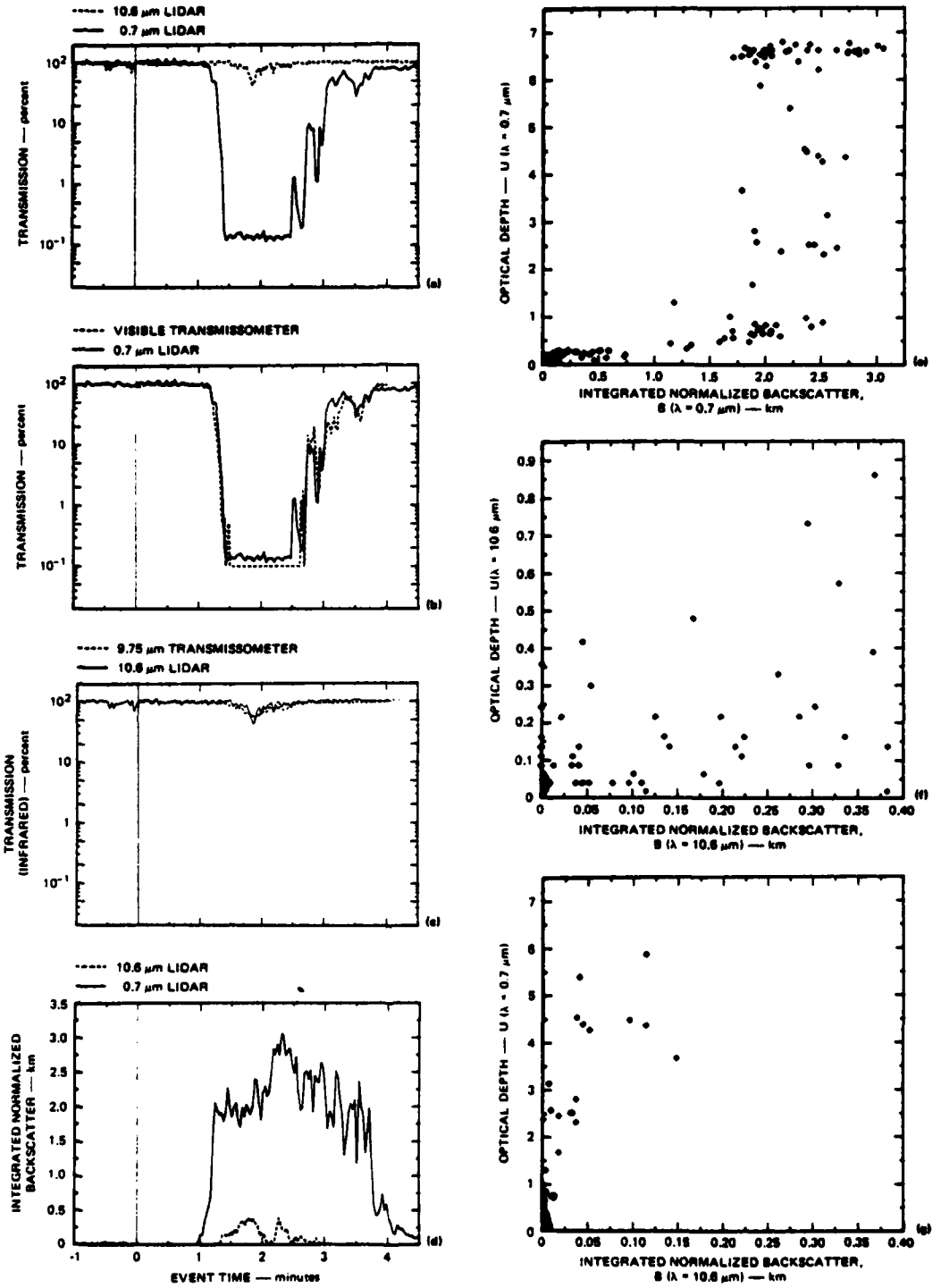

FIGURE 19 TRANSMISSION AND BACKSCATTER DATA PLOTS FOR SMOKE WEEK II, TRIAL 17 (HC)

I. Trial 20

The wavelength dependence of attenuation measured with the two-wavelength lidar system for this phosphorus event (Figure 20) is similar to that observed for the other phosphorus events. However, in this case excellent agreement is obtained between the visible lidar and transmissometer transmission observations, as well as for the infrared records. This indicates that the differences observed between the visible lidar and visible transmissometer during phosphorus events reported earlier were caused by cloud inhomogeneities in the vertical rather than fundamental differences in the measurement techniques. As for other phosphorus events, greater backscatter relative to clear-air backscatter is observed at the visible wavelength, and path-integrated backscatter at the infrared is a better estimator of visible optical depth than is path-integrated backscatter at the visible.

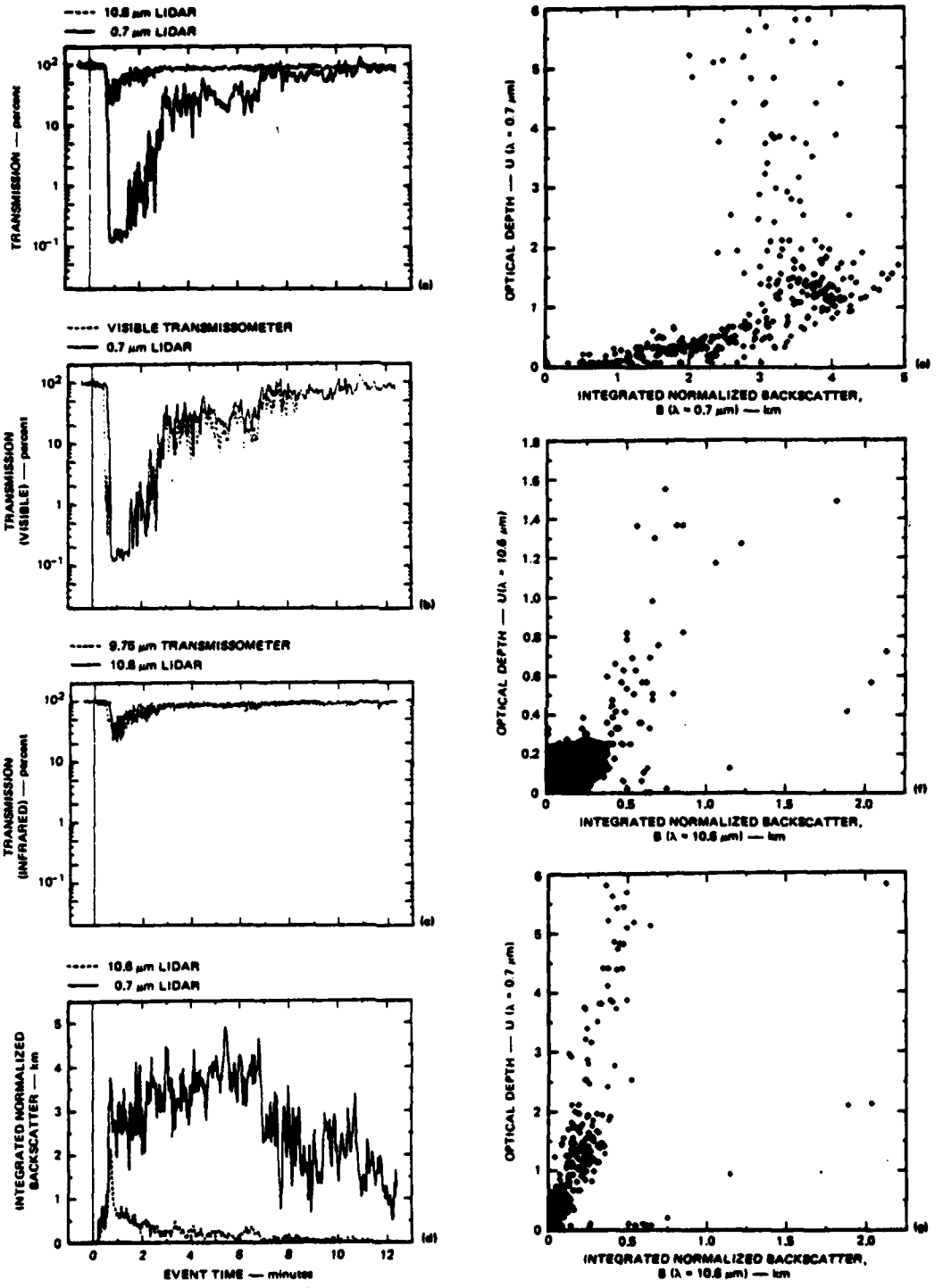

FIGURE 20 TRANSMISSION AND BACKSCATTER DATA PLOTS FOR SMOKE WEEK II, TRIAL 20 (PHOSPHORUS)

J. Trial 21R

Trial 21R was a fog oil experiment. While large attenuation was observed by the visible wavelength lidar, virtually no attenuation was measured by the infrared wavelength lidar (Figure 21a). This is substantiated by the visible and infrared transmissometers (Figure 21b and c). Although greater differences occur in attenuation at the two wavelengths than for phosphorus clouds, less difference is noted in backscatter at the two wavelengths. This behavior indicates that the oil fog consisted of smaller particles with less absorption at the infrared wavelength. The very large degree of data scatter in the plot of backscatter and optical depth values indicates a wide range of particle sizes and shows that integrated backscatter cannot be used as an estimate of cloud attenuation for this type of cloud. The particle size data of University of Tennessee Space Institute (UTSI) indicate particle sizes similar to the phosphorus aerosols, while the Dugway results indicate slightly larger particle sizes.

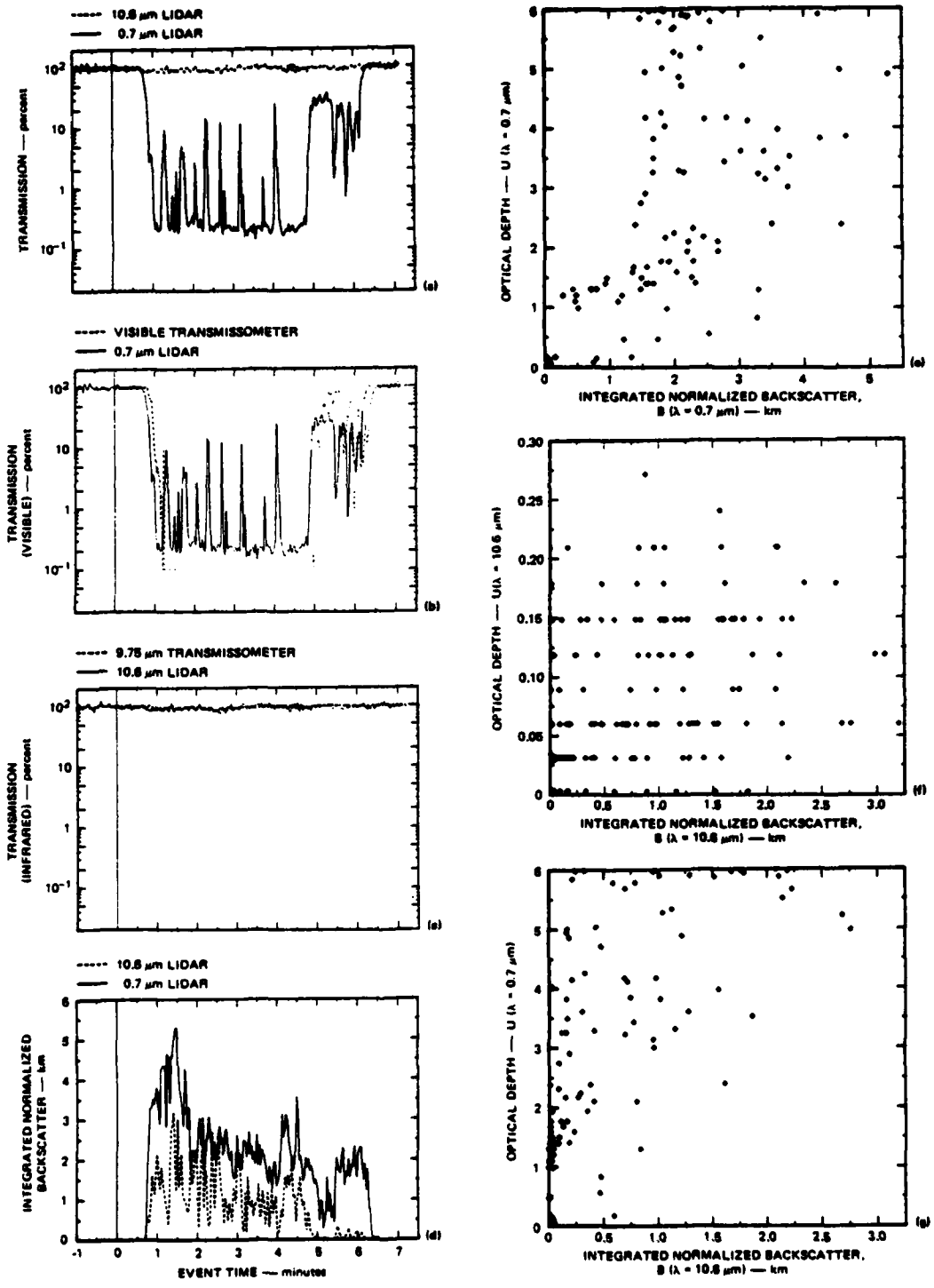

FIGURE 21 TRANSMISSION AND BACKSCATTER DATA PLOTS FOR SMOKE WEEK II, TRIAL 21R (FOG OIL)

K. Trial 22

During Trial 22 (Figure 22) the two-wavelength lidar system made observations of dust generated by vehicular activities. The data presented in Figure 22a show that the dust attenuates visible and infrared laser energy by equal amounts consistent with earlier dust cloud observations conducted at Dugway Proving Ground (Uthe, 1978) and White Sands Missile Range (van der Laan, 1979). These earlier results were explained on the basis of large-sized dust particles. The UTSI particle size data (Table 3) show that the dust particles were larger than for phosphorus, experimental, and oil fog particles by at least a factor of 3. The Dugway data indicate smaller particle size for dust, but this may have resulted because the dust particles were agglomerates that may have been broken up in the sampling tube (Farmer et al., 1979).

The transmission records of the infrared lidar and transmissometer agree better than the records of the visible lidar and transmissometer, indicating larger vertical gradients of dust concentration than in the horizontal downwind direction (see Figure 8).

The lidar-observed normalized backscatter from dust is about twice as great at 0.7 μm than at 10.6 μm. However, since backscatter from clear air was not observed at 10.6 μm, the backscatter-to-clear-air ratio is at least a factor of 2 greater at the visible wavelength. This difference probably results entirely because of the wavelength dependence of backscatter from the clear air.

Infrared and visible integrated backscatter from the dust cloud is a relatively good indicator of attenuation for optical depths of less than 1.5 (transmissions greater than 22 percent). The amount of data scatter in the backscatter-to-optical depth plots is a little less than for the phosphorus and oil fog trials but significantly more than for the experimental particle Trials 4, 5, and 6.

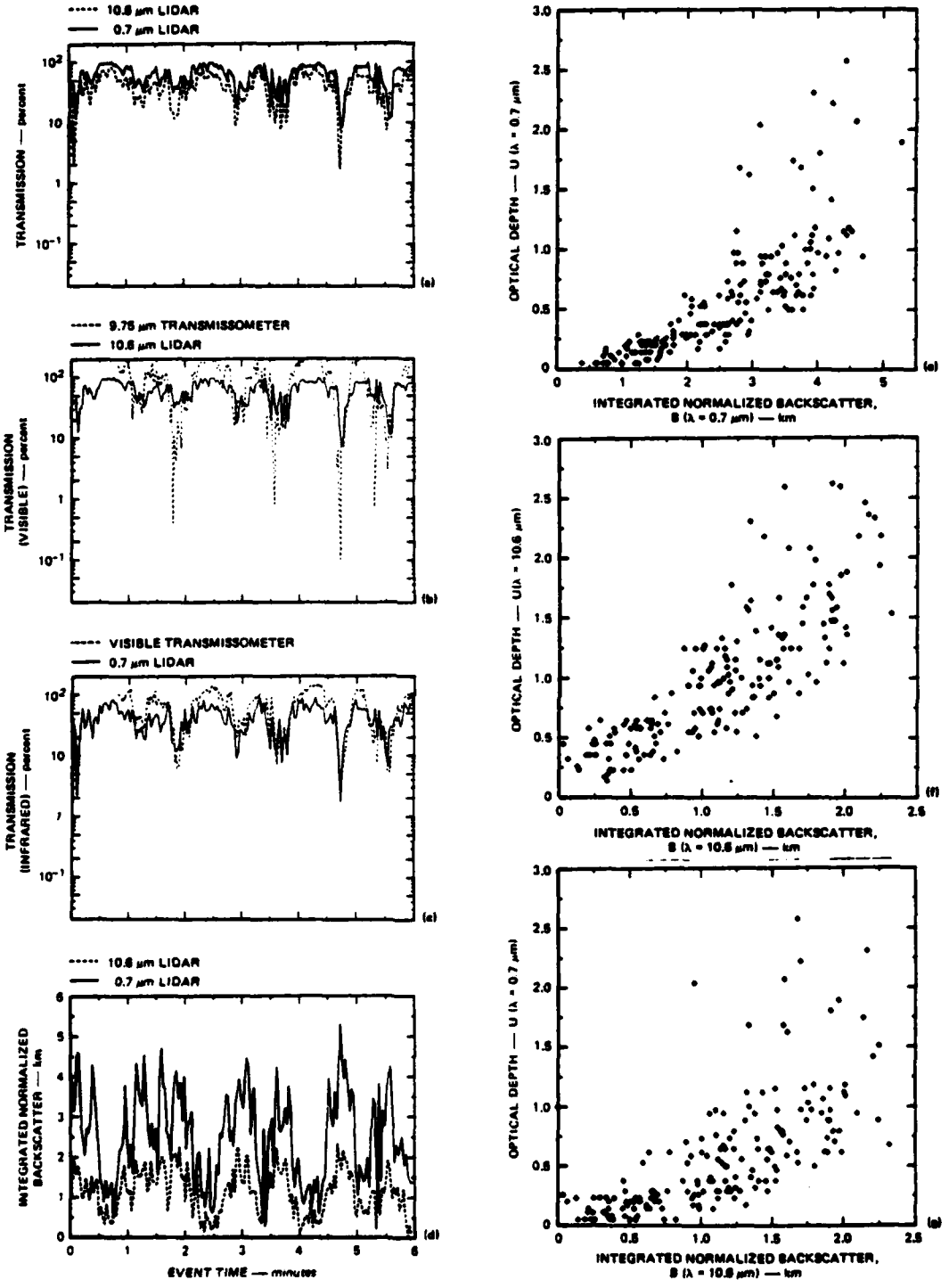

FIGURE 22 TRANSMISSION AND BACKSCATTER DATA PLOTS FOR SMOKE WEEK II, TRIAL 22 (VEHICULAR DUST)

L. Trial 23

Trial 23 (Figure 23) was a dust event generated by the detonation of a high explosive charge (HE). As expected from earlier HE dust tests conducted at Dugway Proving Ground (Uthe, 1978) and White Sands Missile Range (van der Laan, 1979), the dust caused about equal attenuation of the 0.7-μm and 10.6-μm wavelength laser pulses. Relatively good agreement is obtained between the lidar and transmissometer records for both the visible and infrared wavelengths (Figure 23b and 23c). Nearly equal backscatter from the cloud (normalized to clear-air backscatter) was observed at the two wavelengths. Except for the highest values of integrated backscatter, this optical term derived from the lidar signature of the cloud is a relatively good indicator of optical depth for both wavelengths. For relatively low density dust clouds, it appears that path-integrated backscatter at the visible is a better indicator of visible attenuation than is infrared path-integrated backscatter. This was not the case with phosphorus events, as infrared backscatter appeared to be a better indicator than visible backscatter of visible attenuation.

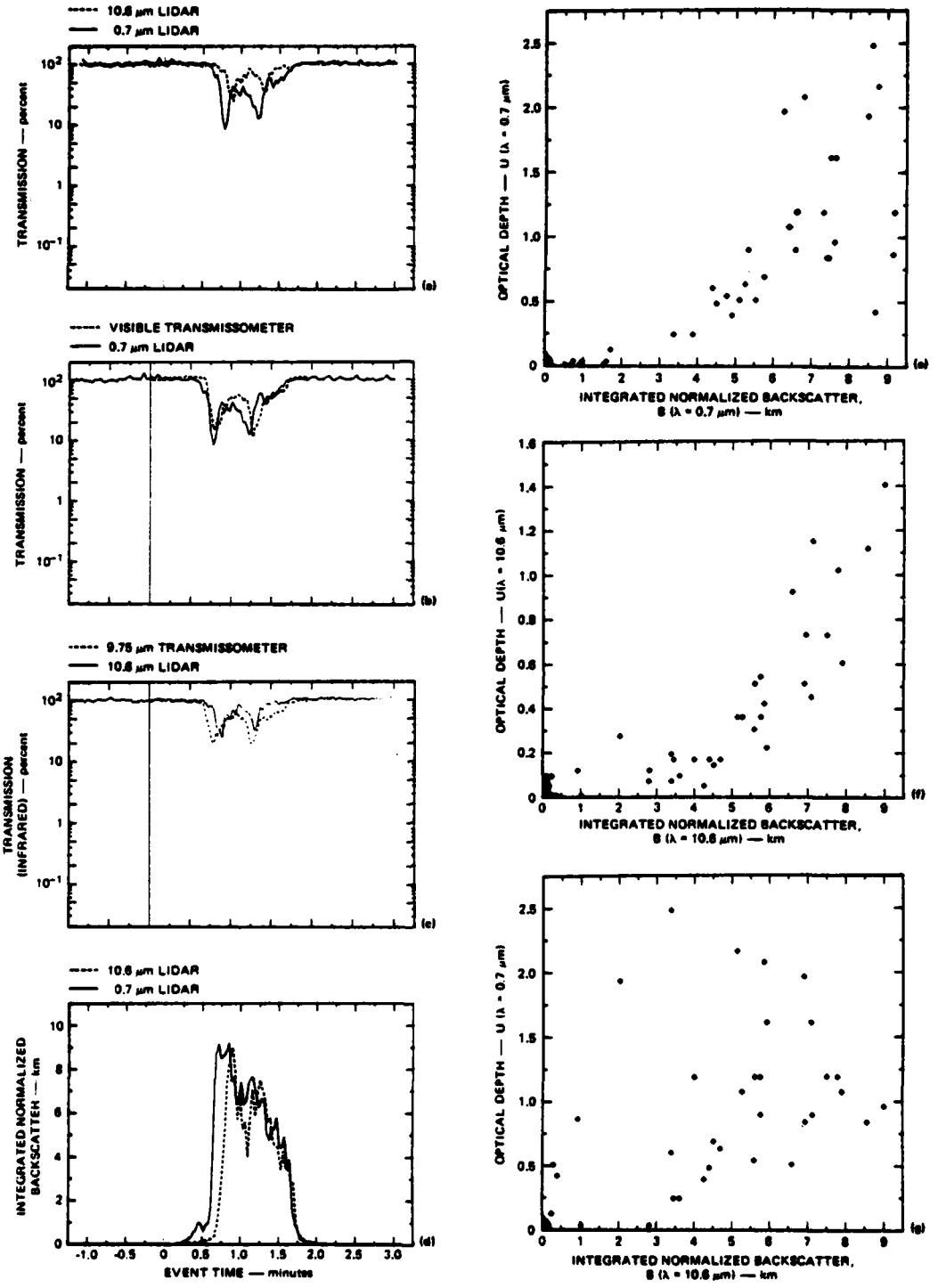

FIGURE 23 ATTENUATION AND BACKSCATTER DATA PLOTS FOR SMOKE WEEK II, TRIAL 23 (HE DUST)

M. Trial 23R

The comments pertaining to Trial 23 hold true for Trial 23R (Figure 24) with the exception that greater backscatter was observed at the infrared lidar wavelength as compared to backscatter observed at the visible wavelength. From Figure 9, it appears that the clear-air backscatter observed during Trial 23R was significantly greater than that observed during Trial 23. Because of the larger wavelength dependence of the clear-air backscatter compared to that of the dust cloud, larger cloud-to-clear-air returns are expected at the infrared wavelength. However, because the infrared detector was not operating at full sensitivity, the clear air was not observed on days with relatively clean air and the infrared dust cloud returns were normalized to the system noise level. Therefore, on hazy days a larger normalized backscatter resulted.

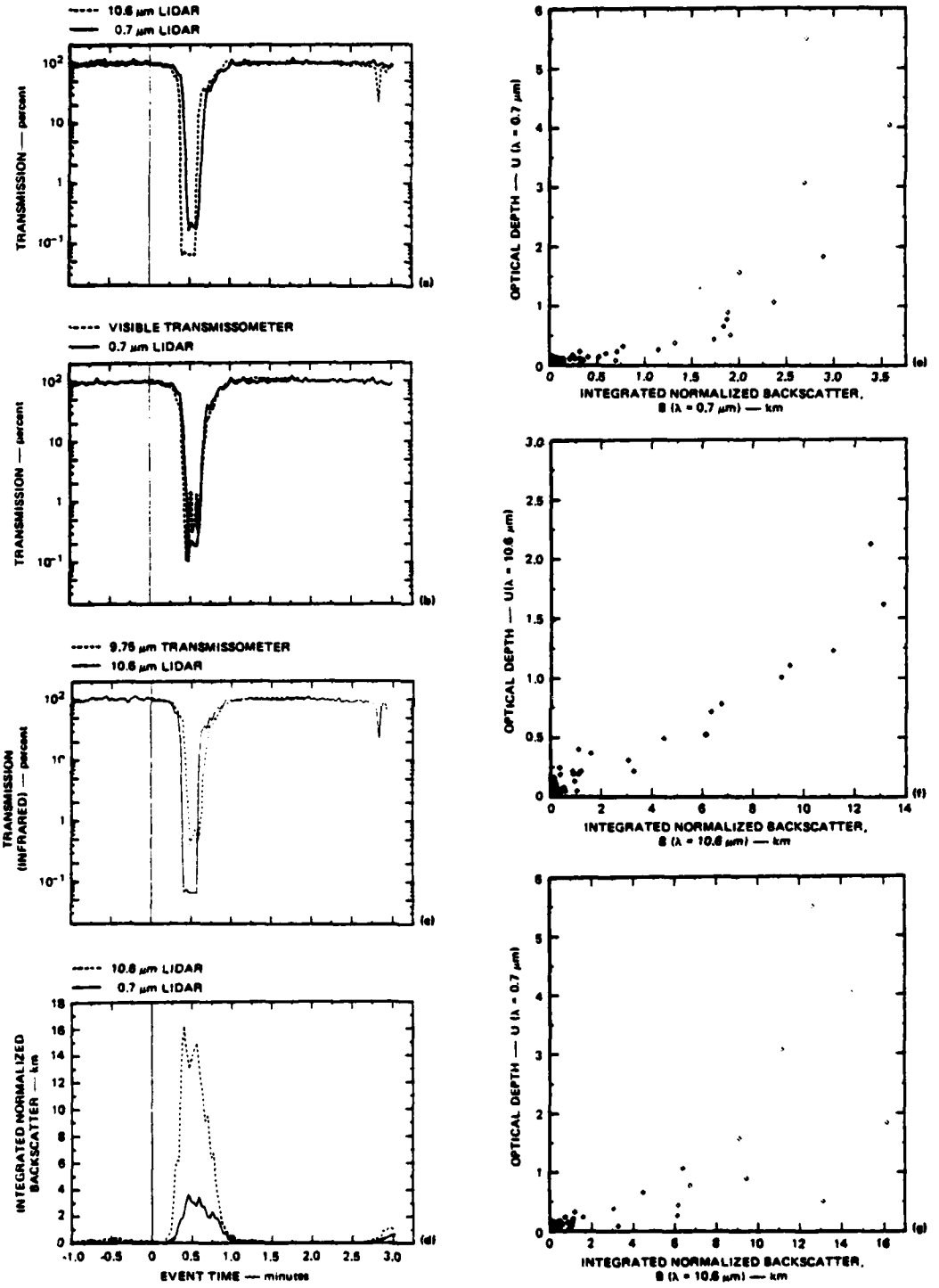

FIGURE 24 ATTENUATION AND BACKSCATTER DATA PLOTS FOR SMOKE WEEK II, TRIAL 23R (HE DUST)

N. Trial 24

Trial 24 (Figure 25) was a phosphorus event. Like the results of the phosphorus events presented earlier in this report, larger attenuation is noted at the visible wavelength as compared to that at the infrared wavelength. Again, as for all other phosphorus events except Trial 20, a significant difference occurs between transmission records derived from the lidar and transmissometer at the visible wavelength, while good agreement is obtained between data from the infrared lidar and transmissometer. As before, this may be explained by the placement of the instruments and large vertical gradients of cloud density for phosphorus events. As for other phosphorus events, infrared backscatter is a better indicator of visible attenuation than is infrared backscatter (Figure 25), although large data scatter occurs for all plots of optical depth against integrated backscatter.

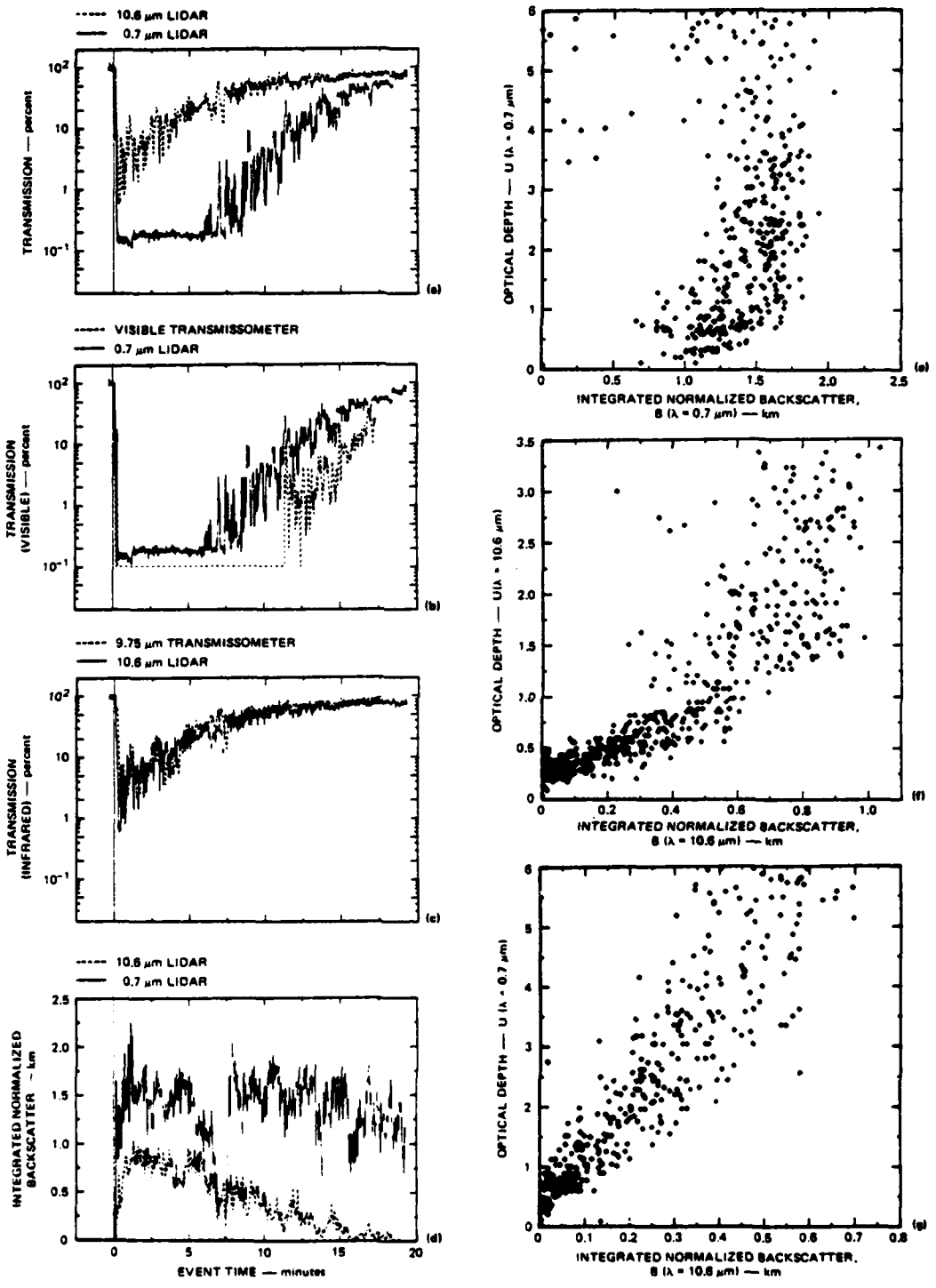

FIGURE 25 ATTENUATION AND BACKSCATTER DATA PLOTS FOR SMOKE WEEK II, TRIAL 24 (PHOSPHORUS)

O. Trial 26

The results for this HE dust event (Figure 26) are very similar to those of Trial 23R. The dust causes nearly equal attenuation of energy at the visible and infrared lidar wavelengths and the lidar and transmissometer records are in good agreement at both wavelengths. The infrared lidar produces a greater cloud backscatter relative to the clear air backscatter, and except for the largest backscatter values, integrated backscatter is a relatively good indicator of attenuation at both visible and infrared wavelengths.

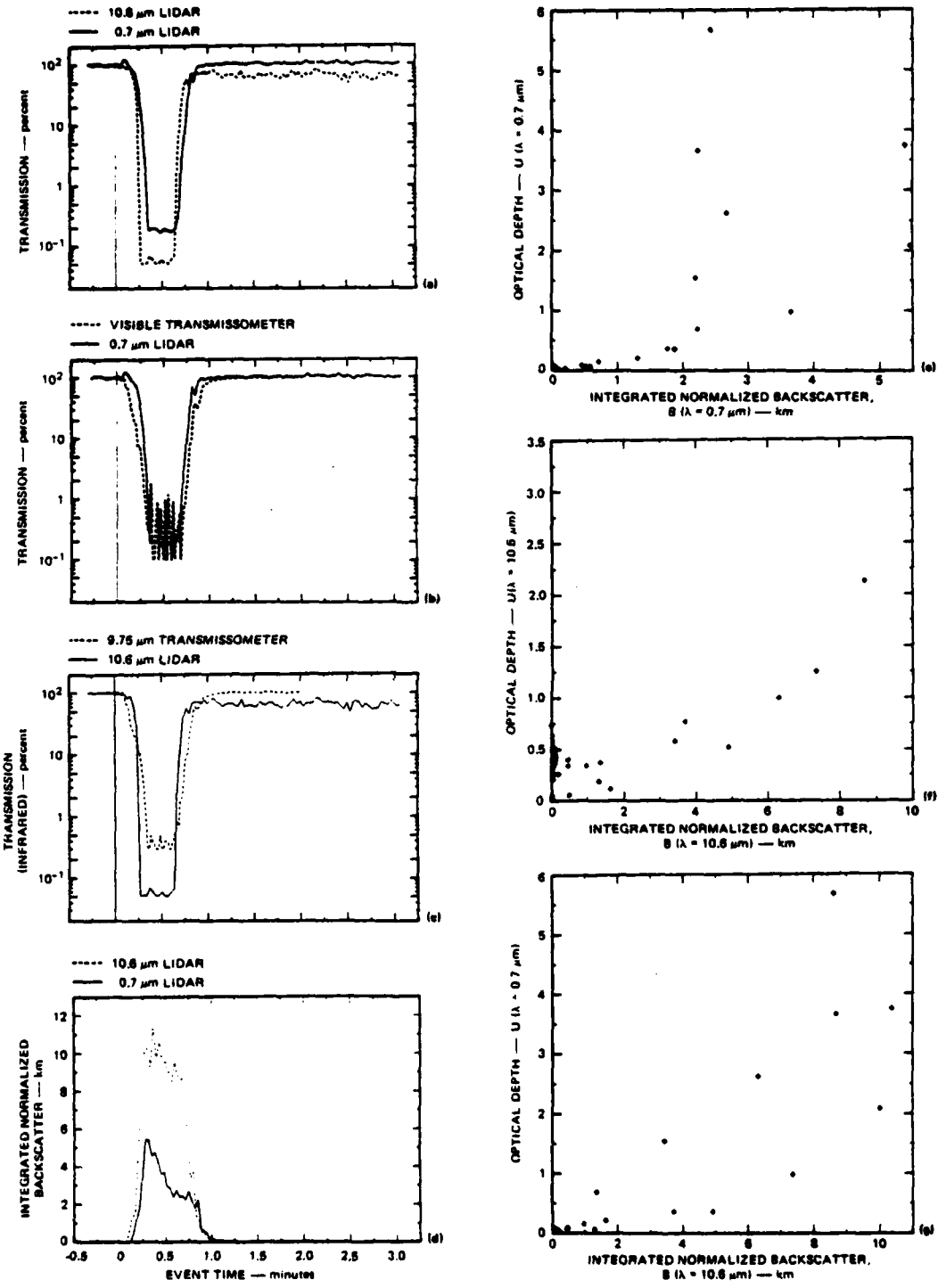

FIGURE 26 ATTENUATION AND BACKSCATTER DATA PLOTS FOR SMOKE WEEK II, TRIAL 26 (HE DUST)

P. Trial 27

The results of Trial 27 (Figure 27) are nearly identical to the results obtained for the other vehicular dust event presented in this report (Trial 22, Figure 22). Excellent agreement between lidar and transmissometer measured attenuation is obtained at both the visible and infrared wavelengths. However, in this test infrared normalized backscatter is larger than visible normalized backscatter, while for Trial 22 the visible backscatter is larger. This is consistent with the results of HE dust tests conducted on 15 November (Trial 23R) as opposed to results obtained on earlier HE dust tests conducted on 11 November (Trial 23) illustrating dependence of normalized backscatter on clear-air density. Integrated backscatter is a relatively good indicator of attenuation at both infrared and visible wavelengths (Figure 27e and 27f), as was the case for Trial 22.

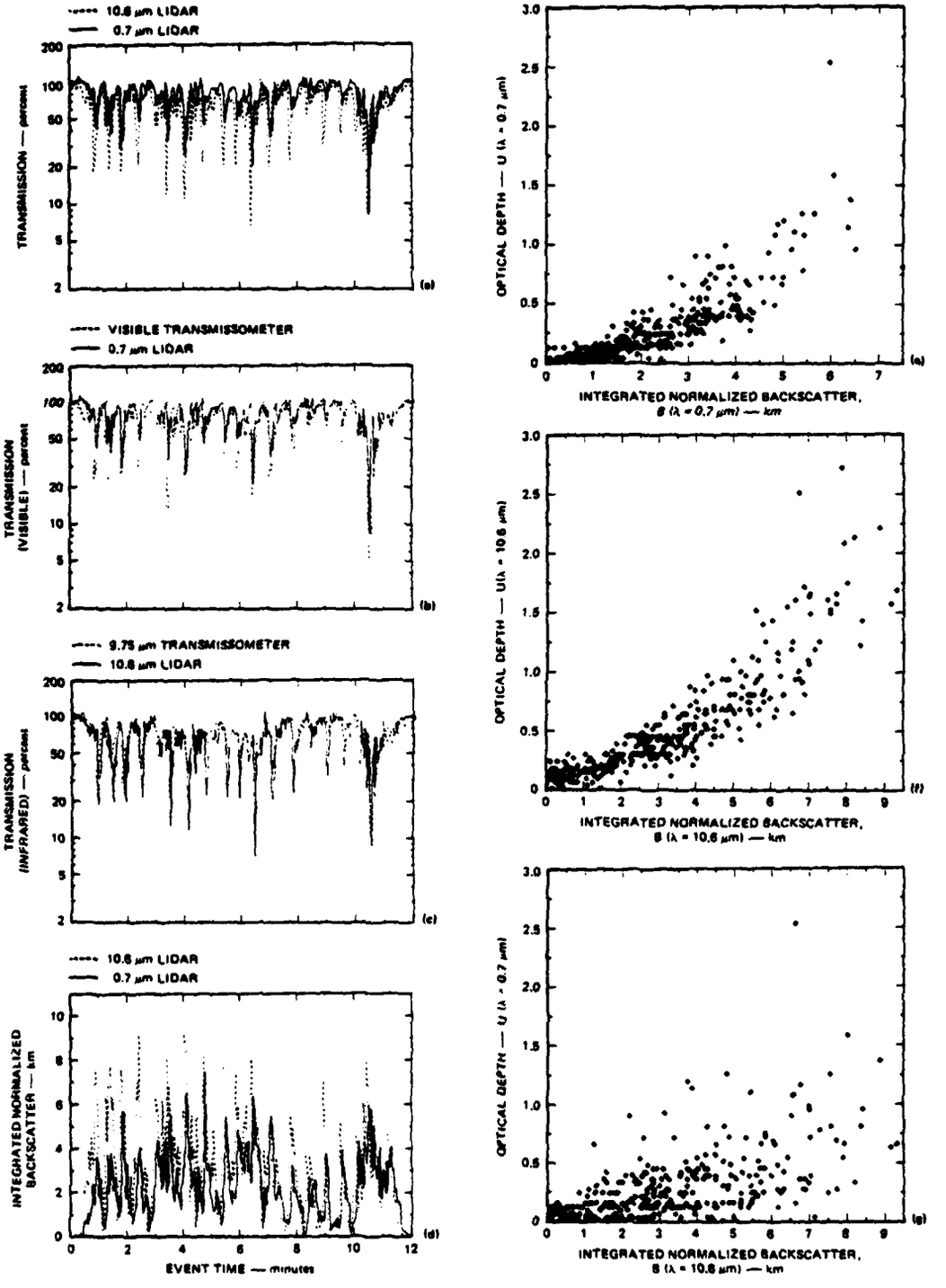

FIGURE 27 ATTENUATION AND BACKSCATTER DATA PLOTS FOR SMOKE WEEK II, TRIAL 27 (VEHICULAR DUST)

VIII SIGNATURE ANALYSIS INTERPRETATION AND IMPLICATIONS

A. Attenuation Estimates Derived from Target Returns

Continuous time records of lidar/target derived attenuation of visible (0.7 μm) and infrared (10.6 μm) energy by Smoke Week II smoke/dust events mostly agree very well with attenuation records derived by independent transmissometer measurements for paths that nearly coincided with lidar-observed paths. Discrepancies between visible lidar and transmissometer records were noted for the phosphorous trials (except Trial 20) and were explained because the lidar and transmissometer paths were located at different elevations (Figure 8) and because of smoke cloud inhomogeneities in the vertical. Nevertheless, the agreement obtained for most observations firmly validates the lidar/target method of measuring cloud attenuation. Although this method requires a passive reflector at the end of the lidar-observed path, the use of multiple reflectors would allow observations over a variety of horizontal paths or for slant paths if elevated targets were installed. For this study, agreement between the lidar and transmissometer records was important because the lidar derived attenuation data can be used to investigate relationships between cloud backscatter and cloud optical density without consideration of cloud inhomogeneities and the spatial offset between the lidar and transmissometer paths.

B. Attenuation Estimates Derived From Cloud Backscatter

The major objective of this study was to determine the feasibility of making attenuation measurements for dense aerosol clouds by analysis of lidar backscatter from the cloud. This method would allow measurements along a variety of nonhorizontal paths through the cloud at different downwind distances from the emission source.

The results presented in Section VII show that data relating cloud path-integrated backscatter and optical depth are widely scattered, but that a relationship can be obtained for most of the Smoke Week II trials. However, at larger values of optical depth the integrated backscatter normally becomes independent of optical depth because backscatter from the far side of the cloud is not observed as it is attenuated by the particles in the near side of the cloud. For several phosphorus trials, integrated backscatter increases with increasing optical depth for small optical depth values, but then decreases with further increases in optical depth. Therefore, both data scatter and non-uniqueness of the optical depth to backscatter relationship must be addressed as limitations of applying the lidar technique for single-ended measurements of cloud attenuation. The data scatter is probably the result of changing particle sizes during cloud development, while the non-unique relationship is a

result of high attenuation and multiple scattering by the very dense aerosol clouds. Derivation of cloud transmission from lidar-observed cloud backscatter is presented below for several Smoke Week II events.

1. Trial 27 (Vehicular Dust)

Figure 28a illustrates a nonlinear expression fitted* to the visible optical depth values (evaluated by the target method) plotted against the visible integrated backscatter for the vehicular dust Trial 27. This expression and observed integrated backscatter values were used to derive a time-dependent record of cloud attenuation. Figure 28b presents this record overplotted with the visible attenuation record obtained with the Dugway transmissometer. Relatively good agreement is obtained between transmissometer and lidar backscatter-derived attenuation records. This agreement indicates that lidar can provide useful measurements of dust cloud attenuation using only backscatter from the cloud and predetermined optical depth-to-integrated-backscatter relation. Alternatively, a scanning lidar could periodically observe a passive reflector to obtain data on the appropriate optical depth-to-integrated-backscatter expression.

Figure 28c presents a plot of the transmissions derived from cloud backscatter plotted against transmissions derived from the target returns only. The best-fit linear relation between these quantities is also plotted on Figure 28c. The slight deviation from a 45° relation indicates that an improved expression may be fitted to the optical depth-to-integrated-backscatter data presented in Figure 28a. The squared linear correlation coefficient (R^2) of 0.80 (80 percent of total variance explained) is obtained by the fit shown in Figure 28c. This linear expression could be used to adjust the backscatter derived transmissions for more perfect agreement with the target return values. Figure 28d presents a plot of the time record of visible transmissions derived from the cloud backscatter in the manner described above overplotted with the transmission record derived from the target returns. The data scatter from the nonlinear expression shown in Figure 28a introduces relatively minor differences in the transmission record shown in Figure 28d.

Figure 29a presents a nonlinear expression fitted to infrared optical depth from target returns plotted against path-integrated backscatter from Trial 27 dust cloud returns. Figure 29b presents the resulting transmission record derived from the infrared backscatter values compared with the Dugway infrared transmission record. As with the visible lidar, the infrared lidar appears to be suitable for making single-ended measurements of dust cloud transmissions providing that the nonlinear expression shown in

*Best fits were found using the IMSL (International Mathematical and Statistical Libraries, Inc., Houston, Texas) Library FORTRAN routine ZXSSQ, which is a finite difference Levenberg-Marquardt scheme for estimating nonlinear parameters.

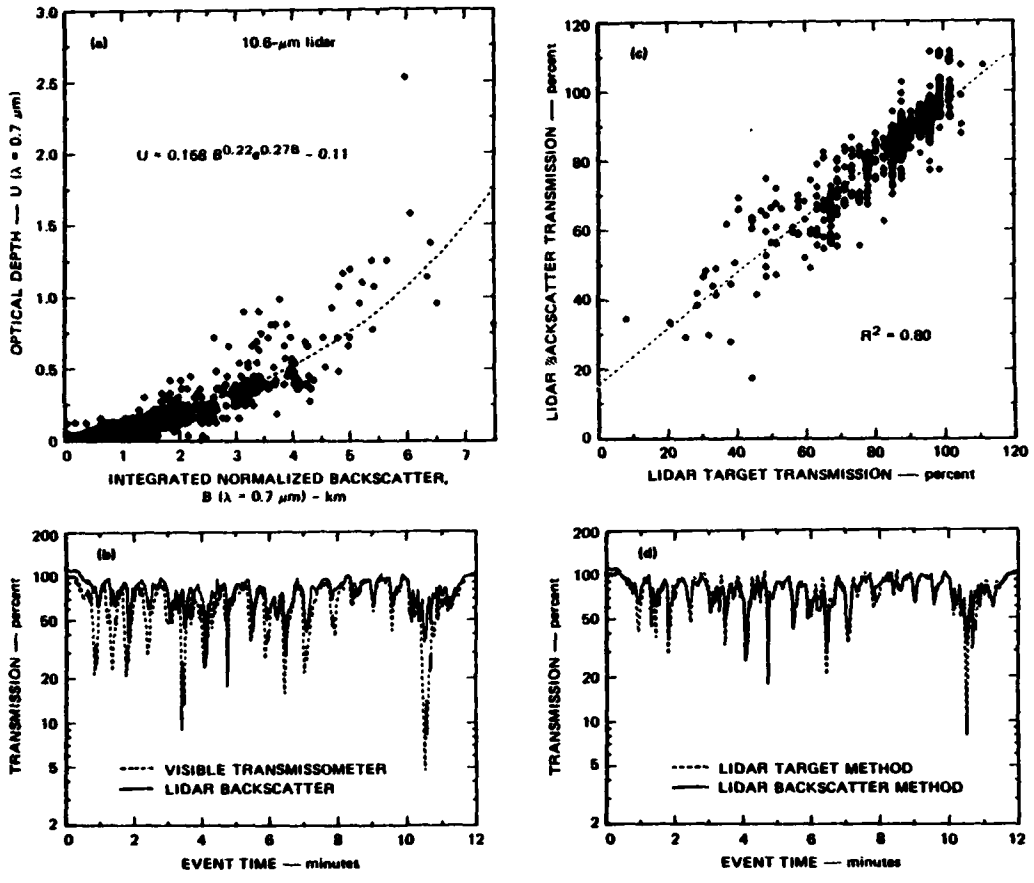

FIGURE 28 DERIVATION OF AN EXPRESSION BETWEEN VISIBLE OPTICAL DEPTH AND INTEGRATED BACKSCATTER, AND COMPARISON OF TRANSMISSION RECORD DERIVED FROM BACKSCATTER DATA WITH TRANSMISSOMETER AND LIDAR TARGET TRANSMISSIONS FOR TRIAL 27 OF SMOKE WEEK II (VEHICULAR DUST)

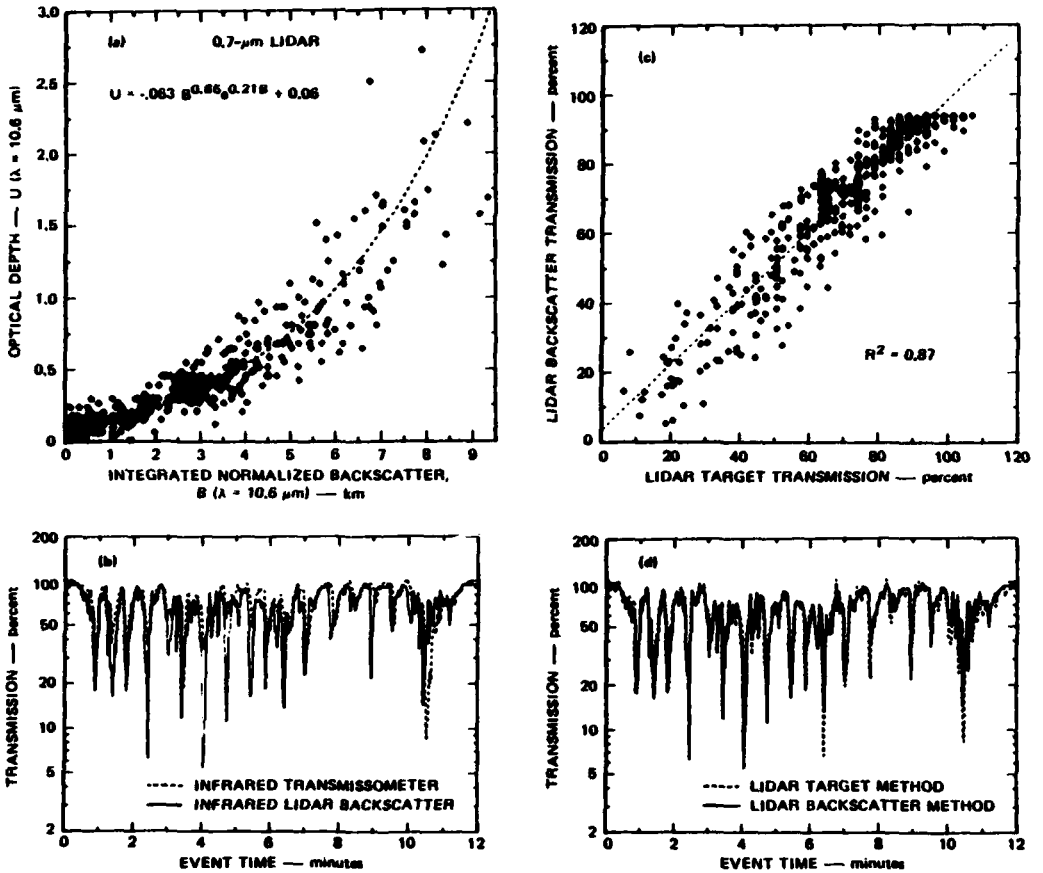

FIGURE 29 DERIVATION OF AN EXPRESSION BETWEEN INFRARED OPTICAL DEPTH AND INTEGRATED BACKSCATTER, AND COMPARISON OF TRANSMISSION RECORD DERIVED FROM BACKSCATTER DATA WITH TRANSMISSOMETER AND LIDAR TARGET TRANSMISSIONS FOR TRIAL 27 OF SMOKE WEEK II (VEHICULAR DUST)

Figure 29a is valid for subsequent observations. The plot of backscatter-derived transmissions against target-derived transmissions shown in Figure 29c indicates that the nonlinear expression shown in Figure 29a is nearly optimal for estimating cloud transmission from cloud backscatter. A plot of lidar target-derived and lidar backscatter-derived transmissions records is shown in Figure 29d.

2. Trial 24 (Phosphorous)

Figures 25e and 25f (Section VII) show that for the Trial 24 phosphorous event the cloud visible optical depth is better estimated from the infrared-integrated backscatter than from the visible-integrated backscatter. Figure 30a illustrates a nonlinear expression for evaluating visible optical depth from infrared integrated backscatter and Figure 30b illustrates a nonlinear expression for evaluating infrared optical depth from the infrared integrated backscatter.

Figure 30c presents a visible transmission record evaluated using the observed infrared backscatter values and the nonlinear expression shown in Figure 30a. Also shown in Figure 30c is the tranmission record determined from the target returns. The infrared transmission record evaluated from the observed infrared backscatter and the expression shown in Figure 30b are presented in Figure 30d. Relatively good correspondence is obtained for both wavelengths, indicating that useful estimates of visible and infrared transmissions for phosphorous clouds can be evaluated from infrared cloud backscatter, providing the expressions shown in Figures 30a and 30b remain valid for other phosphorous clouds.

Comparisons of backscatter-derived transmission records with Dugway transmissometer records are shown in Figures 30e and 30f. The relatively large differences between the lidar and transmissometer records for the visible wavelength was expected, since the target return values also deviated from the Dugway results (Figure 25b), possibly because these instruments observed different elevations through the phosphorous cloud. Nevertheless, the results presented in Figure 30 show that the lidar backscatter method can provide useful optical-density evaluations for paths that cannot easily be observed wtih transmissometers, e.g., slant paths through the cloud.

3. Trial 4 (Experimental Particles)

As a final example of deriving cloud transmission estimates from cloud backscatter, the technique was applied to data collected during Trial 4 (experimental particle cloud). These results are shown in Figure 31. Figure 31a presents a nonlinear fit of visible optical depth evaluated from target returns as a function of visible integrated backscatter from the experimental particle cloud. Figure 31b presents a transmission record derived from visible cloud backscatter plotted with the Dugway transmissometer record. A plot of visible optical depth

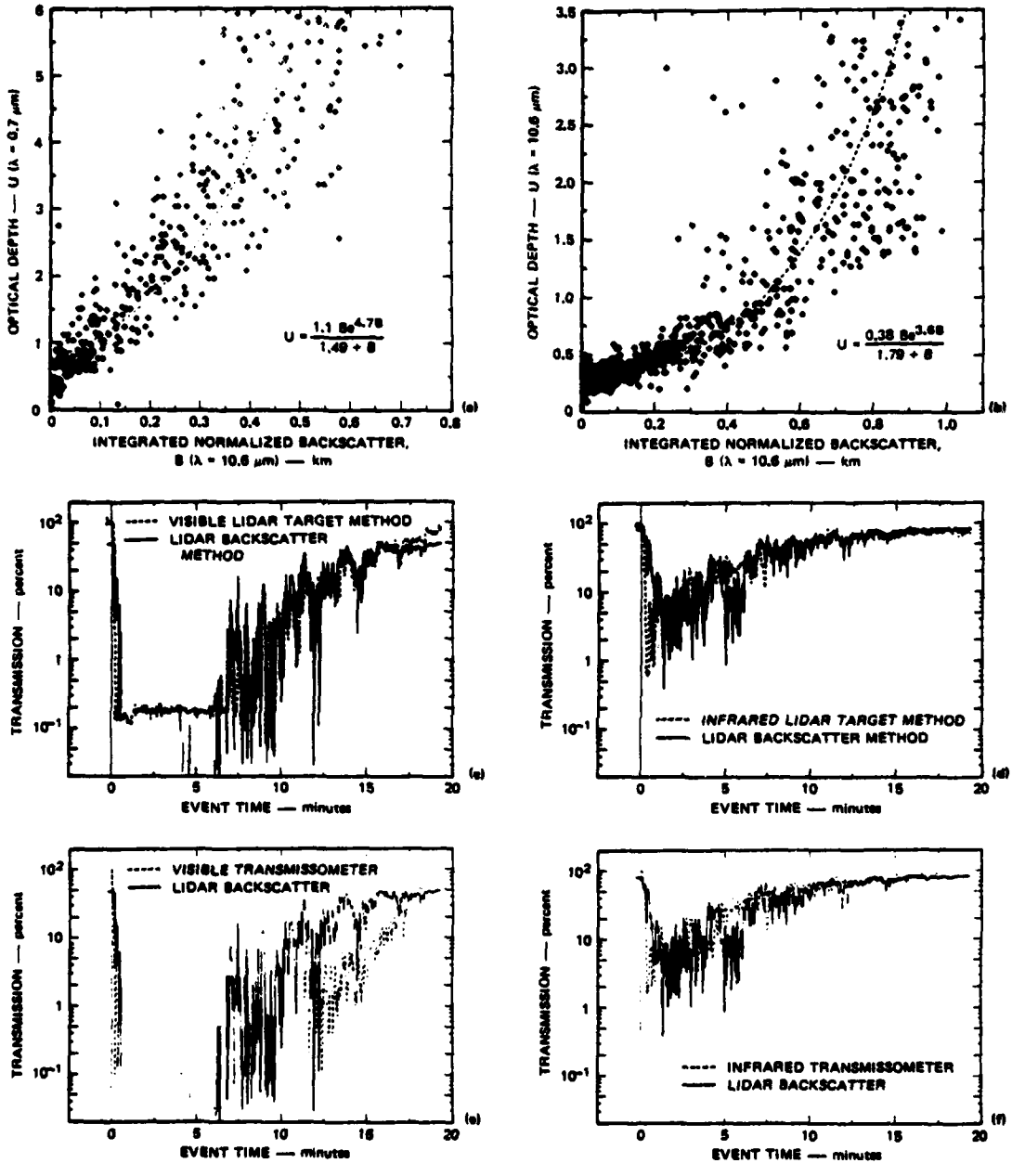

FIGURE 30 DERIVATIONS OF OPTICAL DEPTH-INTEGRATED BACKSCATTER EXPRESSIONS AND COMPARISONS OF DERIVED TRANSMISSIONS

Expressions derived are (a) between visible optical depth and infrared integrated backscatter and (b) between infrared optical depth and infrared integrated backscatter. Comparisons of backscatter-derived transmissions and those derived from lidar target and transmissometer records are shown in (c) through (f).

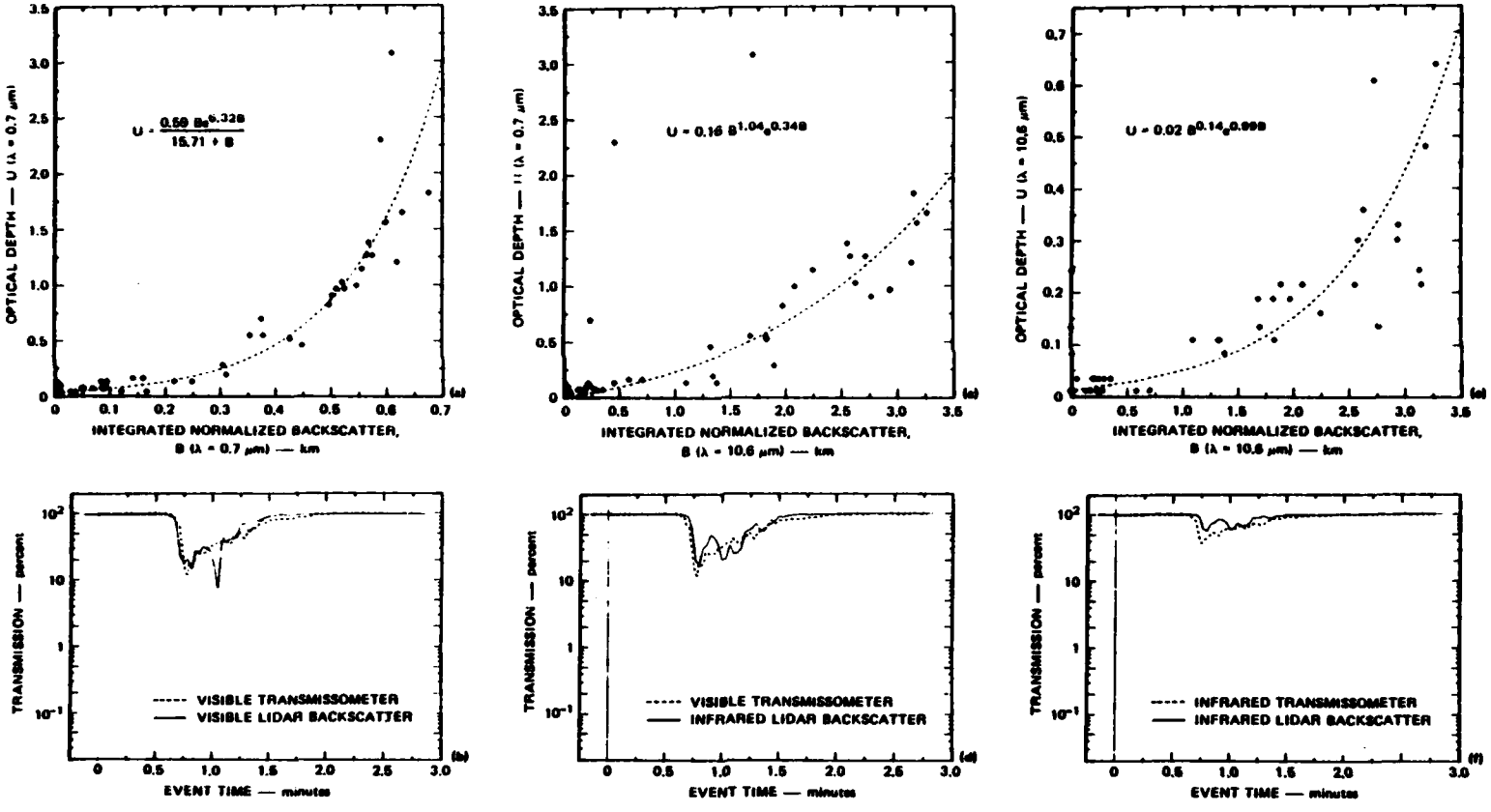

FIGURE 31 EXPRESSIONS RELATING OPTICAL DEPTH TO PATH-INTEGRATED BACKSCATTER FOR SMOKE WEEK II, TRIAL 4 (EXPERIMENTAL PARTICLES) AND RESULTING TRANSMISSION EVALUATIONS COMPARED WITH TRANSMISSOMETER RECORDS

against infrared integrated backscatter (Figure 31c) indicates that visible transmission can also be obtained from the infrared lidar backscatter signature. This is illustrated in Figure 31d, which presents the derived visible transmission record compared with the Dugway visible transmissometer record. Finally, the derivation of an infrared transmission record from the infrared cloud backscatter is shown in Figures 31e and 31f. Relatively good agreement is obtained between lidar and transmissometer attenuation records for all three cases shown in Figure 31.

C. Wavelength Dependence of Attenuation and Backscatter

Table 4 summarizes several features of the two-wavelength lidar observations of phosphorus, HC, experimental, oil fog, and dust clouds. Very large visible attenuation was observed for the phosphorus, HC, and oil fog clouds. With the exception of Trial 23, the HE dust clouds also resulted in large attenuation of visible radiation. Experimental particle and vehicular dust clouds caused substantially less attenuation of visible radiation. The most dramatic difference between visible and infrared attenuation was observed for oil fog (Trial 21R) and HC (Trial 17) with high attenuation in the visible and virtually none in the infrared. Attenuation of the infrared energy is substantially less than attenuation of visible energy for phosphorous clouds, while attenuation at the two wavelengths is about equal for dust clouds and experimental particle Trials 5 and 6. Visible attenuation was greater than infrared attenuation for experimental particle Trial 4.

Visible backscatter was much greater than infrared backscatter for phosphorus and HC clouds, while remaining about equal for dust clouds. It is interesting that infrared backscatter is much greater than visible backscatter for experimental Trial 4 while attenuation is much greater at the visible wavelength. Backscatter at the infrared also greatly exceeds that at the visible wavelength for experimental Trial 5.

The largest data scatter was obtained for the oil fog cloud, with lesser scatter for the phosphorus and HC clouds followed by the dust clouds and finally very little scatter for the experimental clouds. Optical depth related to path-integrated backscatter in the visible was strongly nonlinear for phosphorus and HC clouds and became more linear for the dust and experimental particle clouds. Therefore, the backscatter technique for estimating cloud attenuation is best applied to the dust and experimental particle clouds because of the lesser data scatter and more linear relation between optical depth and path-integrated backscatter.

Table 4

SUMMARY OF LIDAR OBSERVED PARAMETERS

Trial	Obscurant	Optical Depth (OD)			Backscatter (B)			OD/B		Degree of Data Scatter	Degree of Linearity (OD/B)		
		V	IR	V/IR	V	IR	V/IR	V	IR	OD/B	V	IR	V/IR
2	Phosphorous	>6	>5	--	5	0.2	25	>1	>25	L*	--	--	--
3	Phosphorous	>6	1.4	>4	2.5	0.1	25	>2	14	L	S	--	--
7	Phosphorous	>6	2.5	>2.4	3.5	0.3	12	>1	8	L	S	M	L
13	Phosphorous	>6	3.0	>2	5	0.3	17	>1	10	L	M	S	L
20	Phosphorous	>6	1.6	3.7	4	0.3	13	>1	5	L	S	M	L
24	Phosphorous	>6	>5	--	1.5	0.8	2	>4	>6	L	S	M	L
17	HC	>6	0.8	>7.5	2.5	0.3	8	>2	2.7	L	S	--	L
4	Experimental	3	0.6	5	0.6	3	0.2	5	0.2	S	M	M	L
5	Experimental	3	3	1	5	30	0.17	0.6	0.1	S	M	M	--
6	Experimental	0.4	0.25	1.6	6	6	1	0.1	0.4	S	L	L	L
21R	Oil Fog	>6	0.25	>24	4	2	2	>1	0.1	VL	--	--	--
22	Veh Dust	2.5	2.5	1	4	2	2	0.6	1.3	M	M	M	M
27	Veh Dust	1.5	2.0	0.8	4	6	0.7	0.4	0.3	M	L	L	--
23	HE Dust	2.5	1.4	1.8	8	8	1	0.3	0.2	L	M	M	--
23R	HE Dust	>6	2	>3	3	14	0.2	>2	0.1	M	M	L	--
26	HE Dust	>6	>5	--	4	10	0.4	>1	>0.5	M	S	S	M

*VL = very large, L = large, M = medium, and S = small.

IX CONCLUSIONS AND RECOMMENDATIONS

A. Conclusions

The major conclusions of this study are:

(1) Multiple-wavelength lidar systems can provide unique information on the space and time variability of cloud particle distributions and on cloud optical properties.

(2) Lidar provides a means to readily determine the presence of interfering dust during obscurant tests.

(3) Measurements of cloud attenuation derived from the lidar/target method were in excellent agreement with measurements made by conventional two-ended transmissometers for dust and experimental particle clouds. This held true for both visible and infrared wavelengths.

(4) Cloud inhomogeneities in the vertical for phosphorus and HC clouds may have been the cause of discrepancies between the lidar and transmissometer records for this type of smoke, since the optical instruments were located at different elevations. However, good correspondence between the techniques was obtained on one phosphorus event (Trial 20).

(5) Observed data relating path-integrated backscatter and optical depth show a large degree of data scatter with the greatest scatter for oil fog, less scatter for observations of HC and phosphorus smokes, followed by dust clouds and little scatter for experimental particle clouds.

(6) Observed data relating path-integrated backscatter and optical depth shows a nonlinear relation with the greatest nonlinearity for HC and phosphorus smokes and a more linear relationship for dust and experimental particle clouds.

(7) Path-integrated cloud backscatter values used with a nonlinear expression fitted to cloud optical depth data (evaluated from lidar target returns) as a function of integrated backscatter can provide useful estimates of cloud attenuation. This suggests a technique for making transmission measurements over vertical and slant paths through the cloud. As a result of Conclusions 4 and 5 above, the lidar backscatter technique for estimating cloud attenuation is better suited for dust and experimental particle clouds than for oil fog, phosphorus and HC clouds.

(8) Infrared path-integrated backscatter is a better estimator of visible transmission through dense phosphorus clouds than is visible path-integrated backscatter.

(9) Attenuation and backscatter were greater at the visible wavelength (0.7 μm) than at the infrared (10.6 μm) wavelength for HC and phosphorus smokes. For oil fog, attenuation was much greater at visible wavelengths while backscatter was nearly equal at the two wavelengths. Attenuation and backscatter were nearly equal at the visible and infrared wavelengths for dust clouds, while for experimental particle clouds attenuation was nearly equal but backscatter was greater at the infrared wavelength.

B. Recommendations

Based on the results of this study, we feel that the lidar backscatter technique should be further investigated as a means of evaluating optical and physical density of dense aerosol clouds. Specific recommendations are listed below.

(1) An experiment should be designed and conducted to validate the backscatter technique of estimating attenuation of energy propagated along slant paths through dense aerosol clouds. At least two paths through the cloud should be observed with the lidar. One path could be terminated with a passive reflector to provide data on the optical depth-to-integrated-backscatter relation and the other path could be nearly aligned with a transmissometer system to provide a check on backscatter-derived transmissions.

(2) Dense aerosol clouds generated during future optical propagation experiments should be well characterized in terms of particle composition, size, and shape distributions as well as particle concentrations. This information is needed to explain observed wavelength dependance of attenuation and backscatter.

(3) Additional laser wavelengths should be considered. Longer wavelength systems (>15 μm) would result in less attenuation by the scattering particles and therefore a more linear relation between cloud optical depth and integrated backscatter may result as the laser energy would penetrate deeper into the cloud. Studies have shown that an optimum wavelength may exist for relating cloud attenuation and backscatter to cloud density independent of particle size (Pinnick and Jennings, 1980; Uthe, 1980). A wavelength region may exist that would be optimum for reducing the data scatter in plots of optical depth against integrated backscatter. This should be further explored both theoretically and experimentally.

(4) Development of an eye-safe multiple-wavelength lidar would facilitate the observation of dense aerosol clouds over battlefield maneuvers. The lidar could evaluate cloud distribution and optical properties over critical paths for evaluation of cloud effects on weapon systems. Recent advances in generation of from 1- to 16-μm wavelength laser radiation should be considered for this application.

(5) Finally, a repeat of this study but with coaligned lidar and transmissometer paths is suggested in order to eliminate the uncertainties of this study that we feel were introduced by separated lidar and transmissometer paths. Moreover, the nonlinear expressions derived on this study could be used to derive cloud transmission estimates from observed cloud backscatter and these estimates could be related to transmissometer records. Such an experiment should firmly establish the generality of the lidar backscatter technique for a wide range of aerosol types.

REFERENCES

Bowman, V. E., J. Steedman, D. Keefer, W. M. Farmer, and L. J. Pinson, 1979, "Smoke Week II Electro-Optical (EO) Systems Performance in Characterized Obscured Environments at Eglin Air Force Base, FL, Nov. "78 (U)," Special Report from Office of Project Manager Smoke/ Obscurants, DRCPM-SMK-T-001-79. CONFIDENTIAL.

Farmer, W. M., F. A. Schwartz, R. D. Morris, D. Keefer, J. O. Hornkohl, and K. E. Harwell, 1979, "Interferometric Particle Size Measurements During Smoke Week II (U)," Paper B-8 in Proceedings of Smoke/ Obscurants Symposium III, Report No. DRCPM-SMK-T-002-79. CONFIDENTIAL.

Gooley, Walter, Jr., and Howard M. Smalley, 1978, "Smoke Week II Test (U)," Final Report by Dugway Proving Ground, Report No. 7-CO-RD8-DPI-008. CONFIDENTIAL.

Pinnick, R. G. and S. G. Jennings, 1980, "Relationships Between Radiative Properties and Mass Content of Phosphoric Acid, HC, Petroleum Oil, and Sulfuric Acid Military Smokes," Atmospheric Sciences Laboratory Report ASL-TR-0052, U.S. Army Atmospheric Sciences Laboratory, White Sands Missile Range, NM 88002.

Randhawa, J. S. and K. A. Ballard, 1979, "Lidar Measurements During Smoke Week II (U)," Paper B-10 in Proceedings of Smoke/Obscurants Symposium III, Report No. DRCPM-SMK-T-002-79. CONFIDENTIAL.

Smith, Marvin D. and Ping Shih, 1979, "Anomalous Characteristics of Smoke Test Data (U)," Paper A-12 in Proceedings of the Smoke/Obscurants Symposium III, Report No. DRCPM-SMK-T-002-79. CONFIDENTIAL.

Uthe, E. E. and R. J. Allen, 1975, "A Digital Real-Time Lidar Data Recording, Processing, and Display System," Optical and Quantum Electronics, Vol. I, pp. 121-129.

Uthe, E. E., 1978, "Lidar Observations of Smoke and Dust Clouds at 0.7-μm and 10.6-μm Wavelengths," Technical Report 1 issued to U.S. Army Research Office and U.S. Army Atmospheric Science Laboratory, ARO Contract DAAG29-77-C-0001, SRI International, Menlo Park, CA.

Uthe, E. E. 1978, "Remote Sensing of Aerosol Properties Using Laser Radar Techniques," Proceedings of SPIE seminar on Optical Properties of the Atmosphere, Washington, D.C., March 30-31.

Uthe, E. E., 1979, "Lidar Evaluation of Optical and Physical Densities of Dense Aerosol Clouds (U)," Paper B-11 in Proceedings of the Smoke/Obscurants Symposium III, Report No. DRCPM-SMK-T-002-79. CONFIDENTIAL.

Uthe, E. E. 1980, "Evaluation of an Infrared Transmissometer for Monitoring Particulate Mass Concentration of Emissions from Stationary Sources," APCA Journal, Vol. 30, pp. 382-386.

van der Laan, J., 1979, "A System Description of an Improved 10.6-μm Lidar System for Monostatic Optical Measurements of Battlefield Dust and Smoke," Technical Report 2 issued to U.S. Army Research Office and U.S. Army Atmospheric Sciences Laboratory, ARO Contract DAAG29-77-C-0001, SRI International, Menlo Park, CA.

van der Laan, J., 1979, "Lidar Observations at 0.7-μm and 10.6-μm Wavelengths During Dusty Infrared Test 1 (DIRT-1)," Technical Report 3 issued to U.S. Army Research Office and U.S. Army Atmospheric Sciences Laboratory, ARO Contract DAAG29-77-C-0001, SRI International, Menlo Park, CA.

☆U.S. GOVERNMENT PRINTING OFFICE: 1981-0-777-026/10


DAT
FILM